Available online at www.sciencedirect.com
SCIENCE DIRECT®
Comput. Methods Appl. Mech. Engrg. 193 (2004) 2453–2482
Computer methods in applied mechanics and engineering
www.elsevier.com/locate/cma

Finite element method for time dependent scattering: nonreflecting boundary condition, adaptivity, and energy decay

Wolfgang Bangerth [a,*], Marcus Grote [b], Christel Hohenegger [c]

[a] Institute for Computational Engineering and Sciences, University of Texas at Austin, ICES, ACE 5.318, Austin, TX 78712, USA
[b] Department of Mathematics, University of Basel, CH-4052 Basel, Switzerland
[c] School of Mathematics, Georgia Institute of Technology, Atlanta, GA 30332-0160, USA

Received 14 April 2003; received in revised form 13 January 2004; accepted 16 January 2004

Abstract

An adaptive finite element method is developed for acoustic wave propagation in unbounded media. The efficiency and high accuracy of the method are achieved by combining an exact nonreflecting boundary condition [SIAM J. Appl. Math. 55 (1995) 280; J. Comput. Phys. 127 (1996) 52] with space–time adaptivity [East–West J. Numer. Math. 7(4) (1999) 263]. Hence the computational effort is concentrated where needed, while the artificial boundary can be brought as close as desired to the scatterer. Both features combined yield high accuracy and keep the number of unknowns to a minimum. An energy inequality is derived for the initial-boundary value problem at the continuous level. Together with an implicit second order time discretization it guarantees unconditional stability of the semi-discrete system. The resulting fully discrete linear system that needs to be solved every time step is unsymmetric but can be transformed into an equivalent sequence of small nonsymmetric and large symmetric positive definite systems, which are efficiently solved by conjugate gradient methods. Numerical examples illustrate the high accuracy of the method, in particular in the presence of complex geometry.

Keywords: Absorbing boundary conditions; Adaptivity; Energy decay; Wave equation; Acoustic scattering

1. Introduction

We seek an efficient numerical method for the accurate simulation of time-dependent acoustic wave phenomena in unbounded three-dimensional space. Typical applications in acoustic scattering include underwater acoustics, ultra-sound imaging, and remote sensing. As usual we surround the region of interest

* Corresponding author.
E-mail addresses: bangerth@ices.utexas.edu (W. Bangerth), grote@math.unibas.ch (M. Grote), choheneg@math.gatech.edu (C. Hohenegger).

0045-7825/$ - see front matter © 2004 Elsevier B.V. All rights reserved.
doi:10.1016/j.cma.2004.01.021

by an artificial boundary, $\mathscr{B}$, and restrict the computation to the finite spatial domain, Ω, bounded by $\mathscr{B}$. Inside Ω there may be one or more obstacles and source terms, and the acoustic medium may contain inhomogeneities and nonlinearity. To complete the formulation of the problem in Ω, a boundary condition is necessary on $\mathscr{B}$. This boundary condition must absorb outgoing waves at all angles of incidence and frequencies to avoid any spurious reflection from $\mathscr{B}$.

When the continuous formulation is discretized for computation, two independent sources of error appear: the discretization error, due to the numerical scheme inside Ω, and the error at $\mathscr{B}$, due to the artificial boundary condition, or any discrete version of it. To achieve high accuracy at a reasonable cost, any computational method must therefore be able to efficiently control both error components to arbitrarily high accuracy. Thus, it must combine two essential features. First, it must provide space–time adaptivity to resolve geometric singularities, localized source terms, and small scale disturbances propagating through Ω. Second, it must reduce spurious reflection from $\mathscr{B}$ below any desired error tolerance, without incurring prohibitely high computational cost, say, by moving $\mathscr{B}$ farther away from the scatterer. Unless both error components are reduced systematically, the numerical solution will not converge to the solution of the original problem in the unbounded region.

Usually, various approximate boundary conditions are used, which are local differential operators on $\mathscr{B}$. Examples are the conditions by Engquist and Majda [11] and those by Bayliss and Turkel [8]. Although most approximate boundary conditions perform well at nearly normal incidence, their performance degrades rapidly as grazing incidence is approached. In complex situations the scattered waves arrive at the artificial boundary from all interior angles and at all frequencies, so these methods then yield some spurious reflection. Moreover, these errors tend to accumulate with time and prevent accurate long-time integration. To achieve higher accuracy local boundary conditions typically involve increasingly higher derivatives of the solution, which are difficult to implement in a numerical scheme. Hagstrom and Hariharan [20] recently derived an equivalent recursive formulation without high order derivatives.

A different approach to eliminating reflection has been to append an artificial transition layer outside $\mathscr{B}$, which is supposed to absorb outgoing waves. In particular, the popular perfectly matched layer (PML) approach, initially devised by Bérenger for electromagnetic waves [10], was recently adapted to computational acoustics by Qi and Geers [26]. They concluded that "while the PML constitutes an excellent absorbing boundary for plane waves incident upon a planar interface, ... *the PML cannot work well in nonplanar geometries for* $h < 1$ *and* $f < 1$ *because the radiated field/scattered field at intermediate and low frequencies is not purely radiative*." ([26, p. 179], italics present in original)—here f denotes the incident wave frequency and h the distance between the scatter (at $r = 1$) and the PML (at $r = 1 + h$). It then becomes necessary to move $\mathscr{B}$ farther from the region of interest, or to use a thick absorbing layer, to achieve high accuracy.

To avoid the various difficulties mentioned above, we opt for the nonreflecting boundary conditions derived by Grote and Keller [14] for the three-dimensional acoustic wave equation, in the special case when $\mathscr{B}$ is a sphere. It is local in time, nonlocal over $\mathscr{B}$, and exact at all angles of incidence across the entire frequency spectrum. Because it involves only first derivatives of the solution on $\mathscr{B}$, it is easily combined with finite difference [15] or finite element methods [29]. Moreover, far-field evaluation of the solution anywhere outside Ω is straightforward and inexpensive both in computer effort and storage requirement [18]. Nonreflecting boundary conditions were also recently derived for electromagnetic and elastic waves [13,16,17].

As mentioned above, space–time adaptivity is crucial for the efficient numerical simulation of time-dependent acoustic wave phenomena. Indeed, due to the absence of any inherent smoothing mechanism, small scale features in solutions of the wave equation propagate locally through space and time. Adaptive meshes offer the sole practical means for concentrating the computational effort where needed, that is for resolving these small scale features without paying too high a price in CPU time and memory usage. For the wave equation adaptivity and error estimation have been studied extensively, for example by Hughes and Hulbert [21], Johnson [23], Wiberg et al. [25,31], Belytschko and Tabbara [9], Safjan and Oden [27], Issa

et al. [22], and Süli and Wilkins [28]. In contrast to parallel developments in adaptive methods for elliptic problems, however, the significantly more difficult implementation of space–time adaptive methods appears to have prevented their more widespread use for time-dependent applications.

In the implementation of space–time adaptive methods a major difficulty results from the use of local, spatially varying time steps. To avoid this additional complication, we shall base our adaptive numerical scheme on an implicit time discretization of the wave equation, coupled to the nonreflecting boundary condition. By using an implicit, unconditionally stable time discretization we avoid any restrictions due to the CFL condition, which constrains the (global) time step by the (local) smaller mesh size; hence, we apply the same time step across the entire computational domain. The resulting semi-discrete system of equations is then approximated in space by an adaptive finite element strategy. This particular approach is based on a previous implementation described in [6,7], which uses the freely available deal.II finite element library [4,5]. It is similar to the schemes described and analyzed by Aziz and Monk [1], French [12], and Bales and Lasiecka [2]; however, neither adaptivity nor nonreflecting boundary conditions were considered in these references.

To our knowledge, the present work reports on the first attempt to combine space–time adaptivity with a nonreflecting boundary condition. Previous finite difference and finite element implementations of the Grote–Keller boundary condition [14,15,29,30], for instance, always used relatively coarse, equidistant meshes in spherical coordinates, with a few thousand spatial unknowns. In contrast, we shall use here an adaptive discretization with more than 100,000 spatial unknowns, which may change between time steps. Therefore we must use a fully implicit scheme to avoid the implications of small cells on the global time step through the CFL condition. On the other hand, the resulting linear system of equations that needs to be solved every time step now becomes a major challenge. By deriving a nontrivial reformulation of that huge nonsymmetric linear system into small nonsymmetric and large symmetric positive definite systems, we are able to retain the usual efficiency granted by standard conjugate gradient methods. Moreover, by avoiding a discretization in spherical coordinates, we can compute scattering problems from more complicated and realistic geometries. Although we shall base our automatic refinement criterion on a simple smoothness indicator only, more refined techniques based on a posteriori error estimates are possible and envisaged for future work [3].

The layout of the rest of this paper is as follows. In Section 2, we formulate the coupled problem of the wave equation and the nonreflecting boundary condition. In Section 3, the discretization in space and time using adaptive finite elements is presented. The resulting discrete linear system of equations, which needs to be solved at every time step, is nonsymmetric because of the nonreflecting boundary condition. In Section 4, we transform this system into a sequence of symmetric positive definite linear systems, which can be solved efficiently by standard conjugate gradient methods. Energy decay of the solution to the full initial-boundary value problem is shown in Section 5, with some of the more technical proofs postponed to Appendix A. Together with our choice of implicit time discretization, this new result guarantees uniqueness and stability of the semi-discrete problem. Finally in Section 6, we demonstrate the accuracy of our scheme via numerical experiments, even in the presence of complex geometry. These test problems are more challenging than those used in previous studies (see, e.g., [14,15,29,30]), because of their higher frequency content, and therefore more representative of realistic applications.

2. Formulation

We begin with the formulation of the wave equation coupled to the nonreflecting boundary condition. Thus we consider time-dependent acoustic scattering from a bounded scatterer in three-dimensional space. We surround this scattering region by a sphere $\mathscr{B}$ of radius R. Outside $\mathscr{B}$ we assume that the acoustic medium is homogenous and source-free, with constant speed of propagation $c > 0$. In addition, we assume

that the scattered field is confined to the interior of $\mathscr{B}$ at $t = 0$. Outside $\mathscr{B}$, the scattered field u thus satisfies the homogenous acoustic wave equation:

$$\partial_t^2 u - c^2 \Delta u = 0, \quad u(\cdot, 0) = 0, \quad \partial_t u(\cdot, 0) = 0. \tag{1}$$

We suppose that the computational domain Ω within $\mathscr{B}$ is bounded internally by a surface Γ. Furthermore we let $I = (0, T)$ denote the time interval, for which we wish to compute u, and we let $Q_T = \Omega \times I$. In Ω we then consider the following problem:

$$\rho \partial_t^2 u - \nabla a \cdot \nabla u = 0 \quad \text{in } Q_T, \tag{2}$$

$$u = 0 \quad \text{on } \Gamma \times I, \tag{3}$$

$$\left(\partial_r + \frac{1}{c} \partial_t + \frac{1}{R} \right) u = -\frac{1}{R^2} \sum_{n=1}^{\infty} \sum_{m=-n}^{n} (\mathbf{d}_n \cdot \boldsymbol{\psi}_{nm}) Y_{nm} \quad \text{on } \mathscr{B}, \tag{4}$$

$$\frac{\mathrm{d}}{\mathrm{d}t} \boldsymbol{\psi}_{nm} = \frac{c}{R} \mathbf{A}_n \boldsymbol{\psi}_{nm} + \frac{c}{R^2} \mathbf{e}_n (Y_{nm}, u)_{\mathscr{B}} \quad \text{in } I, \tag{5}$$

$$u(\cdot, 0) = u_0 \quad \text{in } \Omega, \tag{6}$$

$$\partial_t u(\cdot, 0) = v_0 \quad \text{in } \Omega, \tag{7}$$

$$\boldsymbol{\psi}_{nm}(0) = 0. \tag{8}$$

Here $\rho > 0$ and $a > 0$ denote the density and the stiffness of the acoustic medium; both can vary with location inside Ω, but must approach constant values in the vicinity of $\mathscr{B}$, with $c = \sqrt{a/\rho}$ in the exterior region.

On $\mathscr{B}$ we introduce the spherical coordinates θ, φ, where $\theta \in [0, \pi]$ corresponds to the angle from the z-axis while $\varphi \in [0, 2\pi)$ corresponds to the polar angle in the (x, y)-plane. Furthermore, let Y_{nm} denote the nmth real spherical harmonic normalized over the unit sphere,

$$Y_{nm}(\theta, \varphi) = \begin{cases} \beta_{nm} \cos m\varphi P_n^{|m|}(\cos\theta) & \text{if} \quad m \leqslant 0, \\ \beta_{nm} \sin m\varphi P_n^{|m|}(\cos\theta) & \text{if} \quad m > 0, \end{cases} \tag{9}$$

with the normalization constants

$$\beta_{nm} = \sqrt{\frac{(2n+1)(n-|m|)!}{2\pi(n+|m|)!}}, \quad m \neq 0, \qquad \beta_{n0} = \sqrt{\frac{(2n+1)}{4\pi}}, \quad m = 0.$$

Hence, every index pair (n, m), with $0 \leqslant n$ and $-n \leqslant m \leqslant n$ corresponds to a distinct spherical harmonic. In (5) the boundary integral over $\mathscr{B}$ corresponds to the L_2-inner product,

$$(Y_{nm}, u)_{\mathscr{B}} = R^2 \int_0^{2\pi} \int_0^{\pi} Y_{nm}(\theta, \varphi) u(R, \theta, \varphi, t) \sin\theta \, \mathrm{d}\theta \, \mathrm{d}\varphi. \tag{10}$$

Eq. (4) is the exact nonreflecting boundary condition, which was derived in [14] and combined with finite differences in [15]; here we have used the improved scaling in inverse powers of R proposed by Thompson and Huan [29]. The boundary condition (4) involves the vector functions $\psi_{nm}(t)$, which are the solutions of the *linear first-order ordinary* differential equation (5). The constant vectors $\mathbf{d}_n, \mathbf{e}_n \in \mathbb{R}^n$ and matrices $\mathbf{A}_n \in \mathbb{R}^{n \times n}$ are defined by

$$(\mathbf{e}_n)_j = \delta_{j1}, \quad (\mathbf{d}_n)_j = \frac{n(n+1)j}{2}, \qquad j = 1, \ldots, n,$$

$$\mathbf{A}_n = \frac{1}{2}\begin{pmatrix} -n(n+1) & -n(n+1) & \cdots & -n(n+1) & -n(n+1) \\ \frac{(n+2)(n-1)}{2} & 0 & \cdots & 0 & 0 \\ 0 & \frac{(n+3)(n-2)}{3} & \cdots & 0 & 0 \\ \vdots & \vdots & \ddots & \vdots & \vdots \\ 0 & 0 & \cdots & 2 & 0 \end{pmatrix}$$
$$= \left[-\frac{1}{2}n(n+1)\delta_{i1} + \frac{(n+i)(n-i+1)}{2i}\delta_{i,j-1} \right]_{i,j=1}^{n}. \tag{11}$$

3. Discretization

To discretize the system of equations (2)–(8), we proceed in three steps:

(1) eliminate second derivatives with respect to time by introducing the additional velocity variable $v = \partial_t u$;
(2) semi-discretize the resulting first-order system in time using the (second-order, implicit) Crank–Nicolson scheme, which guarantees unconditional stability;
(3) discretize in space with finite elements.

By discretizing the wave equation first in time, and then in space, we obtain a discrete formulation that naturally accomodates changing meshes and problem sizes from one time step to another. In contrast, the more common approach of discretizing the equations first in space, and then in time (the method of lines), yields a scheme with a fixed grid and constant number of spatial unknowns. Hence it is ill-suited for adaptive meshes that change as the computation proceeds in time. If the mesh is kept fixed throughout the entire computation, the order of discretization is usually irrelevant.

The resulting discrete algorithm permits to accurately track small disturbances or traveling wave fronts via local refinement, because it allows for meshes that may vary from one time level to another. However, for the sake of efficiency and speed of our method, we do not consider the most general form of space–time adaptivity, which involves local time stepping. Instead we use the same (global) time step across the entire mesh and avoid the usual restrictions, imposed by the CFL condition, by using an implicit method in time. Further details on the choice of the local time step and the adaptive strategy are described in Section 6.1.

We now describe in detail the three steps outlined above that lead to the fully discrete set of equations. First, we introduce the new velocity variable $v = \partial_t u$ and rewrite (2) in the following equivalent form:

$$\rho(\partial_t u - v) = 0 \quad \text{in } \Omega, \tag{12}$$

$$\rho\partial_t v - \nabla \cdot a\nabla u = 0 \quad \text{in } \Omega. \tag{13}$$

Next, we use the Crank–Nicolson scheme to discretize (12), (13) and (3)–(8) in time. This yields the following semi-discrete system of equations at time t_l (superscripts denote time levels) in Ω,

$$\rho(u^l - u^{l-1}) - \frac{k_l}{2}\rho(v^l + v^{l-1}) = 0, \tag{14}$$

$$\rho(v^l - v^{l-1}) - \frac{k_l}{2}\nabla\cdot a\nabla(u^l + u^{l-1}) = 0, \tag{15}$$

together with boundary conditions on $\mathscr{B}$ and a difference equation for the auxiliary variables:

$$\frac{k_l}{2}\left(\partial_r + \frac{1}{r}\right)(u^l + u^{l-1}) + \frac{1}{c}(u^l - u^{l-1}) = -\frac{k_l}{2}\frac{1}{R^2}\sum_{n=1}^{\infty}\sum_{m=-n}^{n} Y_{nm}(\mathbf{d}_n\cdot(\boldsymbol{\psi}_{nm}^l + \boldsymbol{\psi}_{nm}^{l-1})), \tag{16}$$

$$\boldsymbol{\psi}_{nm}^l - \boldsymbol{\psi}_{nm}^{l-1} = \frac{k_l}{2}\frac{c}{R}\mathbf{A}_n(\boldsymbol{\psi}_{nm}^l + \boldsymbol{\psi}_{nm}^{l-1}) + \frac{k_l}{2}\frac{c}{R^2}\mathbf{e}_n(Y_{nm}, (u^l + u^{l-1}))_{\mathscr{B}}. \tag{17}$$

In addition, we have initial conditions $u^0 = u_0$, $v^0 = v_0$, $\boldsymbol{\psi}_{nm}^0 = 0$. $k_l = t_l - t_{l-1}$ denotes the lth time step, which can vary from one time level to the next.

As mentioned above we opt for the implicit Crank–Nicolson method to discretize the wave equation (12), (13) in order to avoid any CFL-restriction on the time step. Yet we also need to discretize the ordinary differential equation (5) for the auxiliary variables $\boldsymbol{\psi}_{nm}(t)$ with the (unconditionally (A-)stable, implicit) Crank–Nicolson method, because the eigenvalues of the matrices $\mathbf{A}_n$ strictly lie in the left half of the complex plane [15]; with increasing n they move farther away from the imaginary axis. Failure to do so would shift the issue from the discretization in the interior to that at the artificial boundary by imposing an additional—and undesirable—restriction on the time step.

To derive a weak form of (14)–(17) we first choose appropriate trial and test function spaces. Thus, we let $H^1_\Gamma = \{v \in H^1 : v|_\Gamma = 0\}$, $\mathscr{R}_\infty = \{\mathbb{R}^n\}_{0\leqslant n,-n\leqslant m\leqslant n}$, $\mathscr{W} = H^1_\Gamma(\Omega)\times L^2(\Omega)\times\mathscr{R}_\infty$, and $\mathscr{T} = L^2(\Omega)\times H^1_\Gamma(\Omega)\times\mathscr{R}_\infty$. Next, we multiply (14)–(17) by test functions $\boldsymbol{\tau}^l = \{\varphi^l, \chi^l, \{\boldsymbol{\zeta}_{nm}^l\}_{0\leqslant n,-n\leqslant m\leqslant n}\} \in \mathscr{T}$, integrate over Ω, and integrate by parts. We add up the resulting equations, which leads to the weak form of the coupled problem at the lth time step:

Find $\mathbf{w}^l = \{u^l, v^l, \{\boldsymbol{\psi}_{nm}^l\}_{0\leqslant n,-n\leqslant m\leqslant n}\} \in \mathscr{W}$ such that

$$b(\mathbf{w}^l, \boldsymbol{\tau}^l) = f(\boldsymbol{\tau}^l) \tag{18}$$

for all test functions $\boldsymbol{\tau}^l \in \mathscr{T}$, with the bilinear form

$$\begin{aligned} b(\mathbf{w}^l, \boldsymbol{\tau}^l) = {} & (\rho u^l, \varphi^l)_\Omega - \frac{k_l}{2}(\rho v^l, \varphi^l)_\Omega + (\rho v^l, \chi^l)_\Omega + \frac{k_l}{2}(a\nabla u^l, \nabla\chi^l)_\Omega \\ & + (\sqrt{a\rho}u^l, \chi^l)_{\mathscr{B}} + \frac{k_l}{2}\frac{1}{R}(au^l, \chi^l)_{\mathscr{B}} + \frac{k_l}{2}\frac{1}{R^2}\sum_{n=1}^{\infty}\sum_{m=-n}^{n}\langle\mathbf{d}_n, \boldsymbol{\psi}_{nm}^l\rangle(aY_{nm}, \chi^l)_{\mathscr{B}} \\ & + \sum_{n=1}^{\infty}\sum_{m=-n}^{n}\left\langle \boldsymbol{\psi}_{nm}^l - \frac{k_l}{2}\frac{c}{R}\mathbf{A}_n\boldsymbol{\psi}_{nm}^l - \frac{k_l}{2}\frac{c}{R^2}\mathbf{e}_n(Y_{nm}, u^l)_{\mathscr{B}}, \boldsymbol{\zeta}_{nm}^l\right\rangle, \end{aligned}$$

and right-hand side

$$\begin{aligned} f(\boldsymbol{\tau}^l) = {} & (\rho u^{l-1}, \varphi^l)_\Omega + \frac{k_l}{2}(\rho v^{l-1}, \varphi^l)_\Omega + (\rho v^{l-1}, \chi^l)_\Omega - \frac{k_l}{2}(a\nabla u^{l-1}, \nabla\chi^l)_\Omega \\ & + (\sqrt{a\rho}u^{l-1}, \chi^l)_{\mathscr{B}} - \frac{k_l}{2}\frac{1}{R}(au^{l-1}, \chi^l)_{\mathscr{B}} - \frac{k_l}{2}\frac{1}{R^2}\sum_{n=1}^{\infty}\sum_{m=-n}^{n}\langle\mathbf{d}_n, \boldsymbol{\psi}_{nm}^{l-1}\rangle(aY_{nm}, \chi^l)_{\mathscr{B}} \\ & + \sum_{n=1}^{\infty}\sum_{m=-n}^{n}\left\langle \boldsymbol{\psi}_{nm}^{l-1} + \frac{k_l}{2}\frac{c}{R}\mathbf{A}_n\boldsymbol{\psi}_{nm}^{l-1} + \frac{k_l}{2}\frac{c}{R^2}\mathbf{e}_n(Y_{nm}, u^{l-1})_{\mathscr{B}}, \boldsymbol{\zeta}_{nm}^l\right\rangle. \end{aligned}$$

We discretize Eq. (18) via Galerkin projection onto finite-dimensional subspaces. For the discretized variables, u_h^l and v_h^l, typical choices for $\mathscr{W}_h^l \subset \mathscr{W}$ and $\mathscr{T}_h^l \subset \mathscr{T}$ include standard finite element spaces, possibly with local h and/or p refinement. For simplicity, we choose $\mathscr{W}_h^l = \mathscr{T}_h^l$. For the auxiliary boundary

variables $\boldsymbol{\psi}^l_{nm,h}$ we choose the finite-dimensional subspace $\mathscr{R}_N \subset \mathscr{R}_\infty$, where $\mathscr{R}_N = \{\mathbb{R}^n\}_{0\leqslant n\leqslant N,-n\leqslant m\leqslant n} \times \{0\}_{n>N,-n\leqslant m\leqslant n}$. With this particular choice for $\mathscr{R}_N$, Galerkin projection effectively truncates the infinite sums over n at some cut-off value N. Therefore, *both the discrete finite element approximation in the interior and the truncation of the infinite sums in the boundary condition correspond to Galerkin projections*. This unifying principle allows for the straightforward derivation of residual-based a posteriori error estimates [3]. The resulting discrete Galerkin formulation reads:

Find $\mathbf{w}^l_h = \{u^l_h, v^l_h, \{\boldsymbol{\psi}^l_{nm,h}\}\} \in W^l_h$ such that

$$b(\mathbf{w}^l_h, \boldsymbol{\tau}^l_h) = f(\boldsymbol{\tau}^l_h) \quad \forall \boldsymbol{\tau}^l_h \in \mathscr{W}^l_h. \tag{19}$$

If we expand the variational formulation (19) with respect to a basis of $\mathscr{W}^l_h$, we obtain the following linear system of equations, which determines the solution at time level t_l:

$$\begin{pmatrix} M & -\frac{k_l}{2}M & 0 & \cdots & 0 \\ \frac{k_l}{2}S + \left(c + \frac{k_l}{2}\frac{c^2}{R}\right)M_{\mathscr{B}} & M & \frac{k_l}{2}\frac{a}{R^2}\mathbf{D}_{00} & \cdots & \frac{k_l}{2}\frac{a}{R^2}\mathbf{D}_{NN} \\ -\frac{k_l}{2}\frac{c}{R^2}\mathbf{E}_{00} & 0 & 1-\frac{k_l}{2}\frac{c}{R}\mathbf{A}_0 & \cdots & 0 \\ \vdots & \vdots & \vdots & \ddots & \vdots \\ -\frac{k_l}{2}\frac{c}{R^2}\mathbf{E}_{NN} & 0 & 0 & \cdots & 1-\frac{k_l}{2}\frac{c}{R}\mathbf{A}_N \end{pmatrix} \begin{pmatrix} \mathbf{U}^l \\ \mathbf{V}^l \\ \boldsymbol{\Psi}^l_{00} \\ \vdots \\ \boldsymbol{\Psi}^l_{NN} \end{pmatrix}$$

$$= \begin{pmatrix} \tilde{M} & \frac{k_l}{2}\tilde{M} & 0 & \cdots & 0 \\ -\frac{k_l}{2}\tilde{S} + \left(c - \frac{k_l}{2}\frac{c^2}{R}\right)\tilde{M}_{\mathscr{B}} & \tilde{M} & -\frac{k_l}{2}\frac{a}{R^2}\mathbf{D}_{00} & \cdots & -\frac{k_l}{2}\frac{a}{R^2}\mathbf{D}_{NN} \\ \frac{k_l}{2}\frac{c}{R^2}\tilde{\mathbf{E}}_{00} & 0 & 1+\frac{k_l}{2}\frac{c}{R}\mathbf{A}_{00} & \cdots & 0 \\ \vdots & \vdots & \vdots & \ddots & \vdots \\ \frac{k_l}{2}\frac{c}{R^2}\tilde{\mathbf{E}}_{NN} & 0 & 0 & \cdots & 1+\frac{k_l}{2}\frac{c}{R}\mathbf{A}_{NN} \end{pmatrix} \begin{pmatrix} \mathbf{U}^{l-1} \\ \mathbf{V}^{l-1} \\ \boldsymbol{\Psi}^{l-1}_{00} \\ \vdots \\ \boldsymbol{\Psi}^{l-1}_{NN} \end{pmatrix}. \tag{20}$$

Here $\mathbf{U}^l$ and $\mathbf{V}^l$ represent the vectors of nodal values of u^l_h, v^l_h, whereas $\boldsymbol{\Psi}^l_{nm} = \boldsymbol{\psi}^l_{nm,h}$. Dots indicate all indices $0\leqslant n\leqslant N$, $-n\leqslant m\leqslant n$. The matrices $\mathbf{A}_n$ are given in (11), and the remaining sub-matrices are defined below (φ^l_i and φ^{l-1}_i denote shape functions at time step l and $l-1$, respectively):

$$M_{ij} = (\rho\varphi^l_i, \varphi^l_j)_\Omega, \quad (M_{\mathscr{B}})_{ij} = (\rho\varphi^l_i, \varphi^l_j)_{\mathscr{B}}, \quad S_{ij} = (a\nabla\varphi^l_i, \nabla\varphi^l_j)_\Omega,$$

$$\tilde{M}_{ij} = (\rho\varphi^l_i, \varphi^{l-1}_j)_\Omega, \quad (\tilde{M}_{\mathscr{B}})_{ij} = (\rho\varphi^l_i, \varphi^{l-1}_j)_{\mathscr{B}}, \quad \tilde{S}_{ij} = (a\nabla\varphi^l_i, \nabla\varphi^{l-1}_j)_\Omega,$$

$$(\mathbf{E}_{nm})_{ij} = (\mathbf{e}_n\mathbf{Y}^{\mathrm{T}}_{nm})_{ij}, \quad (\mathbf{D}_{nm})_{ij} = (\mathbf{Y}_{nm}\mathbf{d}^{\mathrm{T}}_n)_{ij}, \quad (\mathbf{Y}_{nm})_i = (Y_{nm}, \varphi^l_i)_{\mathscr{B}},$$

$$(\tilde{\mathbf{E}}_{nm})_{ij} = (\mathbf{d}_n\tilde{\mathbf{Y}}^{\mathrm{T}}_{nm})_{ij}, \quad (\tilde{\mathbf{Y}}_{nm})_i = (Y_{nm}, \varphi^{l-1}_i)_{\mathscr{B}}.$$

If the underlying computational grid does not change between time levels t_{l-1} and t_l, all quantities with and without tilde coincide. Since the grid changes rather infrequently, say every fifty time steps on a highly refined grid, this is typically the case.

4. Efficient implementation

Lack of efficiency in terms of computational effort and memory requirements is usually perceived as the main drawback of nonreflecting boundary conditions [19]. To address this issue, we shall first show how to decouple the linear system in (20), and thereby devise an efficient solution procedure. Next, we shall compare the run-time and memory complexities of three different strategies for matrix storage.

4.1. Decoupling of the linear system (20)

In previous finite difference or finite element implementations of the Grote–Keller boundary condition [15,29,30], the coupled system of grid variables in the interior domain and auxiliary variables at the artificial boundary was discretized in time first by advancing either type of variables with an explicit method, and then by advancing the other with explicit, implicit, or predictor–corrector methods. While this approach avoids the coupled nature of system (20), the different treatment of the two types of variables appears somewhat arbitrary. It leads to theoretical difficulties for the derivation of a posteriori error estimates, and above all introduces stability conditions on the time step that become more restrictive the finer the mesh or the higher the truncation order N in the nonreflecting boundary condition—see also Section 3. To avoid this undesirable CFL-condition on the time step we use a fully implicit time discretization, while retaining efficiency by deriving an *exact* transformation of the coupled system (20) into an *equivalent* sequence of decoupled linear systems. By solving first for the interior grid variables and then for the auxiliary boundary variables, we thus obtain the *exact* solution of the coupled system, yet without sacrificing the unconditional stability of the scheme. Moreover the decoupled linear systems of equations turn out to be either large, sparse, and symmetric positive definite, which enables the use of standard CG-type iterative methods, or very small, and hence readily invertible by Gaussian elimination. Therefore, the computational effort becomes essentially independent of the truncation order, N, in the nonreflecting boundary condition; our approach yields almost arbitrarily high accuracy on the boundary at a negligible price.

As it stands, the (sparse) linear system of equations in (20) is not particularly amenable to iterative solvers, lacking properties such as symmetry or positive definiteness. Moreover, it is rather large, more than twice the size of the mass matrix M for the single variable U^l, for instance. We shall now show how to decouple this unwieldy linear system and thereby solve for each variable in turn. To begin with the reformulation we multiply the second line of (20) by $\frac{k_l}{2}$, and add the first line to it, which eliminates $\mathbf{V}^l$. Next, we multiply each set of equations for $\mathbf{\Psi}^l_{nm}$ by $-\frac{k_l^2}{4}\frac{a}{R^2}\mathbf{D}_{nm}(I-\frac{k_l}{2}\frac{c}{R}\mathbf{A}_n)^{-1}$, and add it to the previously obtained equation, which eliminates $\mathbf{\Psi}^l_{nm}$. These transformations lead to the following equivalent hierarchy of equations:

$$\begin{aligned}
&\left[M+\frac{k_l^2}{4}S+\left(\frac{ck_l}{2}+\frac{k_l^2}{4}\frac{c^2}{R}\right)M_{\mathscr{B}}+\sum_{n=0}^{N}\sum_{m=-n}^{n}\frac{k_l^3}{8}\frac{a}{R^2}\frac{c}{R^2}\mathbf{F}_{nm}\right]U^l\\
&\quad=\left[\tilde{M}-\frac{k_l^2}{4}\tilde{S}+\left(\frac{ck_l}{2}-\frac{k_l^2}{4}\frac{c^2}{R}\right)\tilde{M}_{\mathscr{B}}-\sum_{n=0}^{N}\sum_{m=-n}^{n}\frac{k_l^3}{8}\frac{a}{R^2}\frac{c}{R^2}\tilde{\mathbf{F}}_{nm}\right]U^{l-1}\\
&\qquad+\tilde{M}V^{l-1}-\sum_{n=0}^{N}\sum_{m=-n}^{n}\frac{k_l^2}{4}\frac{a}{R^2}\mathbf{D}_{nm}\left(I+\left(1-\frac{k_l}{2}\frac{c}{R}\mathbf{A}_n\right)^{-1}\left(I+\frac{k_l}{2}\frac{c}{R}\mathbf{A}_n\right)\right)\mathbf{\Psi}^{l-1}_{nm},
\end{aligned}\tag{21}$$

$$MV^l=\frac{2}{k_l}\left(MU^l-\tilde{M}U^{l-1}\right)-\tilde{M}V^{l-1},\tag{22}$$

$$\mathbf{\Psi}^l_{nm} = \left(I - \frac{k_l c}{2R}\mathbf{A}_n\right)^{-1}\left[\frac{k_l c}{2R^2}\mathbf{E}_{nm}U^l + \frac{k_l c}{2R^2}\tilde{\mathbf{E}}_{nm}U^{l-1} + \left(I + \frac{k_l c}{2R}\mathbf{A}_n\right)\mathbf{\Psi}^{l-1}_{nm}\right]. \tag{23}$$

Here we have introduced the matrices $\mathbf{F}_{nm}$ and $\tilde{\mathbf{F}}_{nm}$ defined by

$$\begin{aligned}\mathbf{F}_{nm} &= \mathbf{D}_{nm}\left(I - \frac{k_l}{2}\frac{c}{R}\mathbf{A}_n\right)^{-1}\mathbf{E}_{nm},\\ \tilde{\mathbf{F}}_{nm} &= \mathbf{D}_{nm}\left(I - \frac{k_l}{2}\frac{c}{R}\mathbf{A}_n\right)^{-1}\tilde{\mathbf{E}}_{nm}.\end{aligned} \tag{24}$$

The transformed system of equations (21)–(23) effectively decouples the variables U^l, V^l, and $\mathbf{\Psi}^l_{nm}$, which can now be determined sequentially and in that order. The computation of V^l in (22) requires the inversion of M, which is symmetric positive definite. The unknowns $\mathbf{\Psi}^l_{nm}$ can be computed independently of one another by solving (23). We remark that the inverse of $(I - \frac{k_l}{2}\frac{c}{R}\mathbf{A}_n)$ is well-defined, since the eigenvalues of A_n strictly lie in the left half of the complex plane (see [15]). Because the $n \times n$ matrices $I - \frac{k_l}{2}\frac{c}{R}\mathbf{A}_n$ are small, typically $n = 1, \ldots, 100$, and only change when the time step size changes, their inversion and storage is negligible. Below, we shall show that the linear system of equations in (21) is also symmetric positive definite. To do so, we prove the following result:

Proposition 1. *Let* $\mathbf{F}_{nm} = \mathbf{D}_{nm}(I - \frac{k_l}{2}\frac{c}{R}\mathbf{A}_n)^{-1}\mathbf{E}_{nm}$. *Then* $\mathbf{F}_{nm} = \alpha_{nm}\mathbf{Y}_{nm}\mathbf{Y}^{\mathrm{T}}_{nm}$ *for some scalar* $\alpha_{nm} > 0$. *The matrices* $\mathbf{F}_{nm}$ *are thus symmetric and positive semi-definite.*

Proof. We insert the definitions for $\mathbf{D}_{nm}$ and $\mathbf{E}_{nm}$ into (24), which implies that $\mathbf{F}_{nm} = \alpha_{nm}\mathbf{Y}_{nm}\mathbf{Y}^{\mathrm{T}}_{nm}$ with

$$\alpha_{nm} = \mathbf{d}_n^{\mathrm{T}}\mathbf{B}_n^{-1}\mathbf{e}_n \quad \text{and} \quad \mathbf{B}_n = I - \frac{k_l}{2}\frac{c}{R}\mathbf{A}_{nm}.$$

Hence the matrices $\mathbf{F}_{nm}$ are symmetric.

We still need to show that $\alpha_{nm} > 0$. To do so, let $\mathbf{z}_n \in \mathbb{R}^n$ denote the solution of

$$\mathbf{B}_n\mathbf{z}_n = \mathbf{e}_n. \tag{25}$$

From the special nonzero patterns of $\mathbf{A}_n$ and $\mathbf{e}_n$, both defined in (11), we observe that

$$z_{n,i} = \frac{k_l c}{4iR}(n+i)(n-i+1)z_{n,i-1}, \quad 2 \leqslant i \leqslant n.$$

By induction we conclude that

$$z_{n,i} = \left[\prod_{j=2}^{i}\frac{k_l c}{4jR}(n+j)(n-j+1)\right]z_{n,1}.$$

Thus all components $z_{n,i}$, $2 \leqslant i \leqslant n$, have the same sign, equal to that of $z_{n,1}$. Next, the first equation in (11) implies that

$$z_{n,1} = \left[1 + \frac{n(n+1)k_l c}{4R}\sum_{i=1}^{n}\prod_{j=2}^{i}\frac{k_l c}{4jR}(n+j)(n-j+1)\right]^{-1} > 0.$$

Therefore the vector $\mathbf{z}_n$ only has strictly positive components, and so does $\mathbf{d}_n$. Since

$$\alpha_n = \mathbf{d}_n^{\mathrm{T}}\mathbf{B}_n^{-1}\mathbf{e}_n = \mathbf{d}_n^{\mathrm{T}}\mathbf{z}_n > 0,$$

α_n is positive, independently of k_l, which completes the proof. □

4.2. Solution procedure

The decoupling described in (21)–(23) shows that every time step involves the subsequent solution of three linear systems:

(1) solve for U^l using (21),
(2) compute (or solve for) V^l using (22),
(3) solve for every $\mathbf{\Psi}^l_{nm}$ using (23).

We shall now discuss each individual step:
Eq. (21) for U^l. The matrix

$$H = M + \frac{k_l^2}{4} S + \left(\frac{c k_l}{2} + \frac{k_l^2}{4} \frac{c^2}{R} \right) M_{\mathscr{B}} + \sum_{n=0}^{N} \sum_{m=-n}^{n} \frac{k_l^3}{8} \frac{a}{R^2} \frac{c}{R^2} \mathbf{F}_{nm}$$

on the left side of (21) is symmetric positive definite. Indeed, the matrices M, S, and $M_{\mathscr{B}}$ are symmetric by construction; moreover, S and $M_{\mathscr{B}}$ are positive semi-definite, while M is positive definite. The matrices $\mathbf{F}_{nm}$ were shown to be symmetric and positive definite in Proposition 1. Therefore the linear system in (21) is symmetric positive definite and can be solved efficiently by a preconditioned conjugate gradient (CG) method. We have found a simple diagonal (Jacobi) preconditioner to be adequate for our purposes, as convergence is typically reached within 20 preconditioned CG iterations.

In practice, the condition number of H does not deteriorate in the presence of the additional terms due to the nonreflecting boundary condition and appears independent of N. In fact, the condition number is usually quite small, even in the presence of strong local mesh refinement. This benign behavior of the condition number is probably linked to the fact that $\mathrm{cond}(M) = \mathrm{O}(1)$, while $\mathrm{cond}(S) = \mathrm{O}(h^{-2})$ yet multiplied by k_l^2, where the time step k_l is of the same order as the mesh size h; all remaining terms are multiplied by higher powers of k_l and thus hardly affect the condition number of H.

Eq. (22) for V^l. In (22) the mass matrix M needs to be inverted. Since $\mathrm{cond}(M) = \mathrm{O}(1)$, as mentioned above, convergence is easily reached, typically within 25 preconditioned CG iterations, even on strongly refined meshes. Moreover, (22) needs to be solved only when the spatial discretization between the previous and the current time steps changes. Otherwise $\tilde{M} = M$, and hence V_l is explicitly given by

$$V^l = \frac{2}{k_l} \left(U^l - U^{l-1} \right) - V^{l-1}.$$

Since we change the mesh rather infrequently, only about every fifty time steps on a highly refined mesh, we seldom need to solve (22).

Eq. (23) for $\mathbf{\Psi}^l_{nm}$. We solve every $n \times n$ nonsymmetric linear system via the LU decomposition of $I - \frac{k_l}{2} \frac{c}{R} \mathbf{A}_n$. Since $1 \leqslant n \leqslant N$, with $N \leqslant 100$, both the size and the number of matrices to be stored remains small and the computational effort involved negligible; moreover, the LU decompositions needs to be recomputed only when the time step, k_l, changes. As a consequence, the numerical effort spent on this part typically is so much smaller than that spent on the solution of (21), that the number of boundary variables $\mathbf{\Psi}^l_{nm}$ hardly affects the total numerical cost.

4.3. Storage and matrix–vector products

At each time step most of the computational effort is spent on the solution of (21), that is on the "inversion" of $H = H_{\mathrm{PDE}} + H_{\mathrm{NBC}}$, where

$$H_{\mathrm{PDE}} = M + \frac{k_l^2}{4} S + \left(\frac{c k_l}{2} + \frac{k_l^2}{4} \frac{c^2}{R} \right) M_{\mathscr{B}}, \quad H_{\mathrm{NBC}} = \sum_{n=0}^{N} \sum_{m=-n}^{n} \frac{k_l^3}{8} \frac{a}{R^2} \frac{c}{R^2} \mathbf{F}_{nm}.$$

Here the $N_\Omega \times N_\Omega$ sparse matrices S and M have the same sparsity pattern, which contains the nonzero entries of $M_{\mathscr{B}}$ (N_Ω denotes the number of degrees of freedom in Ω). In the matrix $M_{\mathscr{B}}$, however, only $N_{\mathscr{B}}$ rows and columns are nonzero, with $N_{\mathscr{B}}$ being the number of degrees of freedom located on $\mathscr{B}$. The matrices $\mathbf{F}_{nm}$ each consist of a (small) full block along $\mathscr{B}$ and hence induce a coupling of all boundary variables there, but are zero elsewhere. Taking into account the nonzero patterns of the various matrices involved, we have identified three different strategies for the storage of H:

(1) Augment the sparsity pattern of H_{PDE} by that of H_{NBC}, and store their sum as one single matrix; then, matrix–vector products with H are standard.
(2) Store H_{PDE} as a sparse matrix of size N_Ω, and H_{NBC} as a dense matrix of size $N_{\mathscr{B}}$. Here multiplication with H_{PDE} is standard, while multiplication with H_{NBC} first requires extraction of the degrees of freedom on $\mathscr{B}$, then a dense matrix–vector multiplication, and finally redistribution to the global vector.
(3) Store H_{PDE} as in (2), but instead of H_{NBC} store only the vectors $\mathbf{Y}_{nm}$ and the scalars α_{nm}. By using the representation $\mathbf{F}_{nm} = \alpha_{nm} \mathbf{Y}_{nm} \mathbf{Y}_{nm}^{\mathrm{T}}$ (Proposition 1), multiplication by H_{NBC} reduces to a sequence of scalar products with all $\mathbf{Y}_{nm}$.

What is the best storage strategy for H, which yields the most efficient matrix–vector product needed for the preconditioned CG iteration? In answering this question we shall distinguish two cases: the fully three-dimensional (3-D) case and the axisymmetric (2.5-D) case. In the 2.5-D case, $N_{\mathscr{B}} = \mathcal{O}(N_\Omega^{1/2})$, while the number of auxiliary functions $\boldsymbol{\psi}_{nm,h}^l$, $1 \leqslant n \leqslant N$, is only N, since $m = 0$ because of symmetry. In the 3-D case, $N_{\mathscr{B}} = \mathcal{O}(N_\Omega^{2/3})$, and the number of auxiliary functions is N^2. However, in the special case that the shape functions on the boundary $\mathscr{B}$ are tensor products of functions in φ and θ, say if a mesh equidistant in φ and θ is used on $\mathscr{B}$, the N^2 vectors $\mathbf{Y}_{nm}$ can be stored as the componentwise product of only $3N + 1$ vectors (one per $1 \leqslant n \leqslant N$ and $-N \leqslant m \leqslant N$), each of length $N_{\mathscr{B}}$; for the third strategy the cost evaluation in the 3-D case will be based on this assumption.

Memory and run-time complexities for the three alternatives are listed in Table 1. Although the complexities of the first two strategies are equal, the second strategy is usually more efficient because the data structures better fit the disparate sparsity patterns of H_{PDE} and H_{NBC}. We remark that both matrix–vector products can be performed independently and in parallel.

As the mesh size h decreases in the interior, the accuracy of the nonreflecting boundary condition simultaneously needs to increase by augmenting N. Since the "wave length" of Y_{nm} is proportional to $\frac{1}{n}$, the value of N should grow at most like $\frac{1}{h}$, that is like $N_\Omega^{1/2}$ in 2.5-D or $N_\Omega^{1/3}$ in 3-D. Therefore the third strategy yields the same overall complexity as the first two, either in 2.5-D, or in 3-D for the case of arbitrary surface meshes; it yields an even smaller complexity of only $\mathcal{O}(N_\Omega)$, if a tensor-product surface mesh is used on $\mathscr{B}$. Moreover for the third strategy, the inner products with Y_{nm} can be performed in parallel. Nevertheless, in our 2.5-D single processor implementation we found that the increase in run-time, due to the N additional

Table 1
Memory and run-time complexities for the three matrix storage strategies: N denotes the point of truncation, N_Ω the number of degrees of freedom, and q the average number of nonzero entries per row in the mass or stiffness matrix

	2.5-D	3-D
Strategies 1 and 2	$\mathcal{O}(qN_\Omega + N_\Omega)$	$\mathcal{O}(qN_\Omega + N_\Omega^{4/3})$
Strategy 3	$\mathcal{O}(qN_\Omega + NN_\Omega^{1/2})$	$\mathcal{O}(qN_\Omega + NN_\Omega^{2/3})$

inner products of length $N_B = N_\Omega^{1/2}$ each, was unacceptably high even for moderate values of $N \geqslant 15$. Hence in our computations, the second strategy was found to yield the best overall performance.

5. Energy decay

The unconditional stability of the implicit time stepping scheme we introduced above hinges on the stability of the underlying initial-boundary value problem (2)–(8). In [15] stability of the continuous problem was proved in the special situation, when the solution admits a decomposition in spherical harmonics not only outside, but also inside Ω, that is in all of $\mathbb{R}^3$. In contrast the result we shall prove in this section uses the decomposition in spherical harmonics only outside Ω. Thus it also applies to situations with a varying velocity field or an arbitrarily shaped obstacle inside Ω. Moreover, we shall determine an explicit energy equality when the sums in the nonreflecting boundary condition extend up to infinity. When the sums are truncated at a finite N, we conclude that the energy remains bounded, and eventually decays, which implies both stability and uniqueness of the solution.

For ease of notation, we assume throughout this section that $a = \rho = 1$ in (2), and hence that $c = 1$, in the exterior domain—this normalization can always be achieved by rescaling space and time; hence, it does not affect the generality of our results.

In the absence of external forces, the energy in the interior of the domain is

$$E(t) = \tfrac{1}{2}\Big(\|\sqrt{\rho}\partial_t u(\cdot,t)\|_\Omega^2 + \|\sqrt{a}\nabla u(\cdot,t)\|_\Omega^2 \Big). \tag{26}$$

Using integration by parts and the wave equation (2), we get

$$\frac{\mathrm{d}}{\mathrm{d}t}E(t) = (\partial_t u(\cdot,t)|_{r=R}, \partial_r u(\cdot,t)|_{r=R})_{\mathscr{B}}. \tag{27}$$

The right side of (27) corresponds to the energy flux across $\mathscr{B}$ due to the nonreflecting boundary condition. We now introduce the decomposition into spherical harmonics at $\mathscr{B}$,

$$u(R,\theta,\varphi,t) = \sum_{n=0}^{\infty}\sum_{m=-n}^{n} u_{nm}(R,t)Y_{nm}(\theta,\varphi),$$

and use the orthonormality of the Y_{nm} to obtain from (27),

$$\frac{\mathrm{d}}{\mathrm{d}t}E(t) = R^2\sum_{n=0}^{\infty}\sum_{m=-n}^{n} [\partial_t u_{nm}(R,t)][\partial_r u_{nm}(R,t)]. \tag{28}$$

Next, we integrate (28) from 0 to T, which yields the energy at $t = T$:

$$E(T) = E(0) + \sum_{n=0}^{\infty}\sum_{m=-n}^{n} I[u_{nm}](T;R). \tag{29}$$

Here we have defined the integral $I_{nm} = I[u_{nm}](T;R)$ as

$$I[u_{nm}](T;R) = R^2\int_0^T [\partial_t u_{nm}(R,t)]\,[\partial_r u_{nm}(R,t)]\,\mathrm{d}t. \tag{30}$$

To show that the energy decays with time we shall show that $I[u_{nm}](T;R) \leqslant 0$ for all $n \geqslant 0$, $|m| \leqslant n$, and $T > 0$. We shall do so below by considering the distinct cases $n = 0$, $n = 1$, and $n > 1$.

$\mathbf{n = 0}$. Multiplication (4) by Y_{00} and integration over $\mathscr{B}$ yields the boundary condition for the zeroth mode:

$$\left(\partial_r + \partial_t + \frac{1}{R}\right) u_{00}(R,t) = 0. \tag{31}$$

We use (31) to replace $\partial_r u_{nm}(R,t)$ in I_{00} from (30), which leads to

$$\begin{aligned} I_{00} &= -R\int_0^T [\partial_t u_{00}(R,t)][u_{00}(R,t)]\,\mathrm{d}t - R^2\int_0^T [\partial_t u_{00}(R,t)]^2\,\mathrm{d}t \\ &= -\frac{R}{2}u_{00}(R,T)^2 - R^2\int_0^T [\partial_t u_{00}(R,t)]^2\,\mathrm{d}t. \end{aligned} \tag{32}$$

Here we have used that $u_{00}(R,0) = 0$. Obviously, $I_{00} \leqslant 0$.

$\mathbf{n} = \mathbf{1}$. Similarly, the boundary condition (4) reduces to

$$\left(\partial_r + \partial_t + \frac{1}{R}\right) u_{1m}(R,t) = -\frac{1}{R^2}\psi_{1m}(t).$$

In addition, the differential equation for ψ_{1m}, and its once differentiated form, read

$$\dot{\psi}_{1m}(t) = -\frac{1}{R}\psi_{1m}(t) + u_{1m}(R,t), \quad \ddot{\psi}_{1m}(t) = -\frac{1}{R}\dot{\psi}_{1m}(t) + \partial_t u_{1m}(R,t).$$

By using these last two equations, while dropping the index $1m$ and the argument (R,t) for simplicity, we obtain

$$\begin{aligned} \partial_r u &= -\partial_t u - \frac{1}{R^2}\psi - \frac{1}{R}u = -\ddot{\psi} - \frac{1}{R}\dot{\psi} - \frac{1}{R^2}\psi - \frac{2}{R}u + \frac{1}{R}u \\ &= -\ddot{\psi} - \frac{1}{R}\dot{\psi} - \frac{1}{R^2}\psi - \frac{2}{R}u + \frac{1}{R}\dot{\psi} + \frac{1}{R^2}\psi \\ &= -\ddot{\psi} - \frac{2}{R}u. \end{aligned}$$

We insert this expression into the definition of I_{1m} and then use the differentiated form above once more to replace $\partial_t u_{1m}$, which yields

$$I_{1m} = -2R\int_0^T u\partial_t u\,\mathrm{d}t - R^2\int_0^T \ddot{\psi}\left(\ddot{\psi} + \frac{1}{R}\dot{\psi}\right)\mathrm{d}t = -R[u(R,T)]^2 - \frac{R}{2}[\dot{\psi}(T)]^2 - R^2\int_0^T \ddot{\psi}^2\,\mathrm{d}t \leqslant 0. \tag{33}$$

$\mathbf{n} > \mathbf{1}$. For higher values of n the argument parallels that with $n = 1$, but the algebra becomes rather complicated. The boundary condition applied at $\mathscr{B}$ to u_{nm} now reduces to

$$\left(\partial_r + \partial_t + \frac{1}{R}\right) u_{nm}(R,t) = -\frac{1}{R^2}\mathbf{d}_n \cdot \boldsymbol{\psi}_{nm}(t), \tag{34}$$

where $\boldsymbol{\psi}_{nm}(t) \in \mathbb{R}^n$ satisfies

$$\frac{\mathrm{d}}{\mathrm{d}t}\boldsymbol{\psi}_{nm} = \frac{1}{R}\mathbf{A}_n\boldsymbol{\psi}_{nm} + u_{nm}(R,t)\mathbf{e}_n, \quad \boldsymbol{\psi}_{nm}(0) = 0, \tag{35}$$

with $\mathbf{d}_n$, $\mathbf{A}_n$, and $\mathbf{e}_n$ defined in (11). Next, we use (34) to replace $\partial_r u_{nm}(R,t)$ in (30), which yields the alternate expression,

$$I_{nm} = -\frac{R}{2}u_{nm}(R,T)^2 - R^2\int_0^T \partial_t u_{nm}(R,t)^2\,\mathrm{d}t - \int_0^T \partial_t u_{nm}(R,t)\,\mathbf{d}_n \cdot \boldsymbol{\psi}_{nm}(t)\,\mathrm{d}t. \tag{36}$$

The sign of the last term on the right of (36) still has to be determined. We now integrate that term by parts, which yields

$$I_{nm} = -\frac{R}{2}u_{nm}(R,T)^2 - R^2\int_0^T \partial_t u_{nm}(R,t)^2\,\mathrm{d}t - u_{nm}(R,T)\,\mathbf{d}_n\cdot\boldsymbol{\psi}_{nm}(T) + \int_0^T u_{nm}(R,t)\mathbf{d}_n\cdot\dot{\boldsymbol{\psi}}_{nm}(t)\,\mathrm{d}t, \tag{37}$$

because $\boldsymbol{\psi}_{nm}(0) = 0$. To proceed we shall now apply the following proposition, whose proof we postpone to the end of this section.

Proposition 2. *For $n \geqslant 1$, let $\boldsymbol{\psi}(t) \in \mathbb{R}^n$ satisfy*

$$\frac{\mathrm{d}}{\mathrm{d}t}\boldsymbol{\psi} = \frac{1}{R}\mathbf{A}_n\boldsymbol{\psi} + u(R,t)\mathbf{e}_n, \quad \boldsymbol{\psi}(0) = 0, \tag{38}$$

with $\mathbf{d}_n$, $\mathbf{A}_n$, and $\mathbf{e}_n$ defined in (4). *Then the integral $I_{nm} = I[u](T;R)$ defined in* (30), *or equivalently in* (36), *satisfies*

$$I_{nm} = -\left(\frac{(n+1)!}{(2n-1)!}\right)^2\frac{(2R)^{2n}}{16}\left[\int_0^T \psi_n^{(n+1)}(t)^2\,\mathrm{d}t + \frac{1}{2R}\sum_{k=0}^{n-1}(2k+1)R^{-2k}\cdot\left(\sum_{j=0}^{k}\psi_n^{(n-j)}(T)\gamma_{kj}R^{k-j}\right)^2 + \frac{n+1}{2R^{2n+1}}\left(\sum_{j=0}^{n}\psi_n^{(n-j)}(T)\gamma_{nj}R^{n-j}\right)^2\right], \tag{39}$$

where $\psi_n^{(n-j)}(t)$ denotes the $(n-j)$th derivative of the nth component of $\boldsymbol{\psi}(t)$, $\boldsymbol{\psi} = [\psi_1,\ldots,\psi_n]^{\mathrm{T}}$, and

$$\gamma_{nj} = \frac{(n+j)!}{(n-j)!j!2^j}. \tag{40}$$

For every u_{nm}, $1 \leqslant n \leqslant N$, Eq. (4) reduces to (34). Thus, we can directly apply Proposition 2 to u_{nm} in (36). Since all the terms on the right of (39) involve squared quantities, we immediately conclude that

$$I_{nm} \leqslant 0, \quad n \leqslant N.$$

For all higher Fourier modes, $n > N$, the boundary condition applied at $\mathscr{B}$ to u_{nm} reduces to the (approximate) first-order Bayliss–Turkel [8] condition,

$$\left(\partial_r + \partial_t + \frac{1}{R}\right)u_{nm}(R,t) = 0, \quad n > N, \tag{41}$$

which coincides with (31), with u_{00} replaced by u_{nm}. As a consequence, the derivation in (32) applies equally well to I_{nm}, for $n > N$. Thus we have shown that $I_{nm} \leqslant 0$ for all $n \geqslant 0$, $|m| \leqslant n$, which implies via (29) that the energy remains bounded in time. We summarize this result as a theorem.

Theorem 1. *Let u solve* (2) *with* (4) *truncated at $n = N$. Then the energy $E(t)$, defined in* (26), *satisfies*

$$E(T) \leqslant E(0), \quad T \geqslant 0,$$

for arbitrary N.

Remark. The energy estimate in Theorem 1 implies the uniqueness of (sufficiently regular) solutions of (2)–(4). Furthermore it establishes the stability of the fully coupled problem, regardless of the shape of the scatterer Γ or the point of truncation N. In fact the energy strictly decreases, that is $E(t) < E(0)$, as soon as any Fourier coefficient $(Y_{nm}, u(\cdot,t))_{\mathscr{B}}$ becomes nonzero, that is upon first arrival at $\mathscr{B}$.

If the sums in (4) are not truncated at N, but instead extend up to infinity, the exact boundary condition is applied to every u_{nm}. Then Proposition 2 actually provides the following *energy equality*:

Corollary 1. *Let u solve* (2) *with a, ρ, and c equal to one outside Ω. Then the energy* $E(t)$, *defined in* (26), *satisfies*

$$E(T) = E(0) - \frac{R}{2}u_{00}(R,T)^2 - R^2\int_0^T \partial_t u_{00}(R,t)^2\,\mathrm{d}t + \sum_{n=1}^{\infty}\sum_{m=-n}^{n} I[u_{nm}](T;R), \tag{42}$$

with $I[u_{nm}](T;R) = I_{nm}$ *given by* (39).

We conclude this section with the proof of Proposition 2.

Proof (Proposition 2). The case $n = 1$ was proved above. Indeed, direct verification shows that (32) is identical to (39) for $n = 1$.

For $n = 2, 3$ we shall prove that (36) coincides with (39) by direct computation, whereas for $n \geqslant 4$ we shall proceed by induction over n.

$\mathbf{n = 2}$. Since $\mathbf{d}_2 = [3,6]^{\mathrm{T}}$, Eq. (37) now reduces to

$$\begin{aligned} I_{2m} = &-\frac{R}{2}u(R,T)^2 - R^2\int_0^T u_t(R,t)^2\,\mathrm{d}t - u(R,T)(3\psi_1(T) + 6\psi_2(T)) \\ &+ \int_0^T u(R,t)(3\dot{\psi}_1(t) + 6\dot{\psi}_2(t))\,\mathrm{d}t, \end{aligned} \tag{43}$$

where we have dropped indices for simplicity. For $n = 2$, the 2×2 system of ordinary differential equation (38) becomes

$$\begin{pmatrix} \dot{\psi}_1(t) \\ \dot{\psi}_2(t) \end{pmatrix} = \frac{1}{R}\begin{pmatrix} -3 & -3 \\ 1 & 0 \end{pmatrix}\begin{pmatrix} \psi_1(t) \\ \psi_2(t) \end{pmatrix} + u(R,t)\begin{pmatrix} 1 \\ 0 \end{pmatrix}. \tag{44}$$

Again, we now replace in (43) all instances of $u(R,t)$ and $u_t(R,t)$ by using (44), and thus rewrite (43) as

$$\begin{aligned} I_{2m} = &-\frac{R}{2}\dot{\psi}_1(T)^2 - \frac{27}{2R}\psi_1(T)^2 - \frac{45}{2R}\psi_2(T)^2 - 6\dot{\psi}_1(T)\psi_1(T) - 9\dot{\psi}_1(T)\psi_2(T) \\ &- \frac{36}{R}\psi_1(T)\psi_2(T) - 6\int_0^T \dot{\psi}_1(t)^2\,\mathrm{d}t + 6\int_0^T \dot{\psi}_1(t)\dot{\psi}_2(t)\,\mathrm{d}t \\ &+ \frac{18}{R}\int_0^T \psi_1(t)\dot{\psi}_2(t)\,\mathrm{d}t + \frac{9}{R}\int_0^T \psi_2(t)\dot{\psi}_1(t)\,\mathrm{d}t + \frac{9}{R}\int_0^T \dot{\psi}_1(t)\psi_1(t)\,\mathrm{d}t \\ &+ \frac{18}{R}\int_0^T \psi_2(t)\dot{\psi}_2(t)\,\mathrm{d}t - R^2\int_0^T \ddot{\psi}_1(t)^2\,\mathrm{d}t - 9\int_0^T \dot{\psi}_2(t)^2\,\mathrm{d}t \\ &- 6R\int_0^T \ddot{\psi}_1(t)\dot{\psi}_1(t)\,\mathrm{d}t - 6R\int_0^T \ddot{\psi}_1(t)\dot{\psi}_2(t)\,\mathrm{d}t - 18\int_0^T \dot{\psi}_1(t)\dot{\psi}_2(t)\,\mathrm{d}t. \end{aligned} \tag{45}$$

We integrate the second, third, and fourth term in (45) by parts, and explicitly evaluate the fifth, sixth, and ninth integral. Then, we use the second equation in (44) to express $\psi_1(t)$, $\dot\psi_1(t)$, and $\ddot\psi_1(t)$ in terms of $\psi_2(t)$ and its higher derivatives. These calculations lead to

$$\begin{aligned} I_{2m} = &-\frac{7R^3}{2}\ddot\psi_2(T)^2 - 6R^2\ddot\psi_2(T)\dot\psi_2(T) - 18R\dot\psi_2(T)^2 - 3R\ddot\psi_2(T)\psi_2(T) \\ &-\frac{27}{2R}\psi_2(T)^2 - 9\dot\psi_2(T)\psi_2(T) - 6R^2\int_0^T \ddot\psi_2(t)^2\,\mathrm{d}t - 9\int_0^T \dot\psi_2(t)^2\,\mathrm{d}t \\ &- R^4\int_0^T \dddot\psi_2(t)^2\,\mathrm{d}t - 6R\int_0^T \dddot\psi_2(t)\,\mathrm{d}t - 18\int_0^T \ddot\psi_2(t)\psi_2(t)\,\mathrm{d}t \\ &- 9\int_0^T \dot\psi_2(t)^2\,\mathrm{d}t - 6R^2\int_0^T \dddot\psi_2(t)\dot\psi_2(t)\,\mathrm{d}t. \end{aligned} \tag{46}$$

We now integrate by parts all remaining integrals in (46) to obtain

$$\begin{aligned} I_{2m} = &-R^4\int_0^T \dddot\psi_2(t)^2\,\mathrm{d}t - \frac{7}{2}R^3\ddot\psi_2(T)^2 - 15R\dot\psi_2(T)^2 - \frac{27}{2R}\psi_2(T)^2 \\ &- 12R^2\ddot\psi_2(T)\dot\psi_2(T) - 9R\ddot\psi_2(T)\psi(T) - 27\dot\psi_2(T)\psi_2(T). \end{aligned} \tag{47}$$

Finally, we combine terms to form squares in (47) and rewrite (48) as

$$\begin{aligned} I_{2m} = &-R^4\int_0^T \dddot\psi_2(t)^2\,\mathrm{d}t - \frac{3}{2R}\left(3\psi_2(T) + 3R\dot\psi_2(T) + R^2\ddot\psi_2(T)\right)^2 \\ &-\frac{3R}{2}\left(\dot\psi_2(T) + R\ddot\psi_2(T)\right)^2 - \frac{R^3}{2}\ddot\psi_2(T)^2. \end{aligned} \tag{48}$$

Direct verification again shows that (48) coincides with (39) for $n = 2$.

n = 3. The argument for $n = 3$ parallels that for $n = 2$; hence, we omit details and simply state the main steps of the proof. Again, we replace all instances of $u(R,t)$ and $u_t(R,t)$ in (37) with $n = 3$ by using the first equation in (38) with $n = 3$. From the second and third equations in (38), we then express $\psi_1(t)$ and $\psi_2(t)$ only in terms of $\psi_3(t)$ and its derivatives. Finally, integration by parts and combination of terms to form squares yields (39) with $n = 3$.

n ⩾ 4, *induction step*. We assume that (39) holds for n and shall now show that it also holds for $n + 1$. To begin we rewrite the first equation in (38) as

$$u(R,t) = \dot\psi_1(t) + \frac{n(n+1)}{2}\frac{1}{R}\sum_{j=1}^{n}\psi_j(t). \tag{49}$$

Here we have dropped indices from u_{nm} and $\boldsymbol{\psi}_{nm}$ for simplicity—recall that $\psi_k(t)$ denotes the kth component of the n-vector function $\boldsymbol{\psi}_{nm}(t)$. In (49) we now evaluate the scalar product $\mathbf{d}_n \cdot \dot{\boldsymbol{\psi}}(t)$ and replace both $u(R,t)$ and $u_t(R,t)$ by using (49). Then we extract all terms involving $\psi_1(t)$ from the sums, so that all sums now start at $j = 2$. These calculations lead to

$$
\begin{aligned}
I_{nm} = &-\frac{R}{2}\dot{\psi}_1(T)^2 - R^2\int_0^T \ddot{\psi}_1(t)^2\,\mathrm{d}t + \left(\frac{n(n+1)}{2}\right)^2\Bigg[-\frac{1}{R}\psi_1(T)^2 - \frac{2}{R}\psi_1(T)\sum_{j=2}^{n}\psi_j(T)\\
&-\frac{1}{R}\left(\sum_{j=2}^{n}\psi_j(T)\right)^2 - \frac{1}{R}\psi_1(T)\sum_{j=2}^{n} j\psi_j(T) - \frac{1}{R}\sum_{j=2}^{n}\psi_j(T)\sum_{j=2}^{n} j\psi_j(T)\\
&+\frac{1}{R}\sum_{j=2}^{n} j\int_0^T \psi_1(t)\dot{\psi}_j(t)\,\mathrm{d}t + \frac{1}{R}\sum_{j=2}^{n}\int_0^T \dot{\psi}_1(T)\psi_j(t)\,\mathrm{d}t + \frac{1}{R}\int_0^T \sum_{j=2}^{n}\psi_j(t)\sum_{j=2}^{n} j\dot{\psi}_j(t)\,\mathrm{d}t\\
&-\int_0^T \dot{\psi}_1(t)^2\,\mathrm{d}t - 2\sum_{j=2}^{n}\int_0^T \dot{\psi}_1(t)\dot{\psi}_j(t)\,\mathrm{d}t - \int_0^T\left(\sum_{j=2}^{n}\dot{\psi}_j(t)\right)^2\mathrm{d}t\Bigg]\\
&+\frac{n(n+1)}{2}\Bigg[-2\dot{\psi}_1(T)\psi_1(T) - \dot{\psi}_1(T)\sum_{j=2}^{n}\psi_j(T) - \dot{\psi}_1(T)\sum_{j=2}^{n} j\psi_j(T) + \int_0^T \dot{\psi}_1(t)^2\,\mathrm{d}t\\
&+\sum_{j=2}^{n} j\int_0^T \dot{\psi}_1(t)\dot{\psi}_j(t)\,\mathrm{d}t - R\dot{\psi}_1(T)^2 - 2R\sum_{j=2}^{n}\int_0^T \ddot{\psi}_1(t)\dot{\psi}_j(t)\,\mathrm{d}t\Bigg].
\end{aligned}
\tag{50}
$$

We integrate by parts all integrals in (50), except the sixth, tenth, and those which involve squared quantities. In the resulting expression, we again seek to replace every $\psi_j(t)$, $j = 1,\ldots,n-1$, in terms of $\psi_n(t)$ and its higher derivatives. To do so, we note that the last $n-1$ equations in (38) imply that

$$
\psi_j(t) = \frac{R}{a_{j+1}}\dot{\psi}_{j+1}(t) = \cdots = \frac{R^{n-j}}{a_{j+1}\cdots a_n}\psi_n^{(n-j)}(t), \quad j = 1,\ldots,n-1.
$$

Hence, from Lemma 1 (Appendix A) we conclude that

$$
\psi_j(t) = R^{n-j}2^n\gamma_{nj}\frac{n!}{(2n)!}\psi_n^{(n-j)}(t), \quad j = 1,\ldots,n-1. \tag{51}
$$

For ease of notation, we shall now restrict ourselves to the case $R = 1$. We use (51) in (50) (with $R = 1$) to replace every $\psi_j(t)$, $j = 1,\ldots,n-1$, in terms of $\psi_n(t)$ and its higher derivatives. This yields

$$
\begin{aligned}
I_{nm} = &-\left(\frac{n!2^n}{(2n)!}\right)^2\gamma_{n1}^2\int_0^T \psi_n^{(n+1)}(t)^2\,\mathrm{d}t + \left(\frac{n!2^n}{(2n)!}\right)^2\Bigg\{-\frac{n^2+n-2}{2}\gamma_{n1}^2\psi_n^{(n)}(T)^2\\
&-\gamma_{n1}^2\left(\psi_n^{(n)}(T) + \frac{n(n+1)}{2}\psi_n^{(n-1)}(T)\right)^2 - \frac{1}{2}\left(\gamma_{n1}\psi_n^{(n)}(T) + \frac{n(n+1)}{2}\cdot\sum_{j=2}^{n}\psi_n^{(n-j)}(T)\gamma_{nj}\right)^2\\
&-\left(\frac{n(n+1)}{2}\right)^2\Bigg[\int_0^T\left(\sum_{j=2}^{n}\psi_n^{(n-j+1)}(t)\gamma_{nj}\right)^2\mathrm{d}t\\
&+\gamma_{n1}\sum_{j=2}^{n}\left\{\gamma_{nj}\int_0^T \psi_n^{(n-1)}(t)\psi_n^{(n-j+1)}(t)\,\mathrm{d}t + j\gamma_{nj}\int_0^T \psi_n^{(n)}(t)\psi_n^{(n-j)}(t)\,\mathrm{d}t\right\}\\
&+\int_0^T \sum_{j=2}^{n}\gamma_{nj}\psi_n^{(n-j+1)}(t)\sum_{j=2}^{n} j\gamma_{nj}\psi_n^{(n-j)}(t)\,\mathrm{d}t + \gamma_{n1}\psi_n^{(n-1)}(T)\sum_{j=2}^{n}\gamma_{nj}\psi_n^{(n-j)}(T)
\end{aligned}
$$

$$+ 2\gamma_{n1}\sum_{j=2}^{n}\gamma_{nj}\int_0^T \psi_n^{(n)}(t)\psi_n^{(n-j+1)}(t)\,\mathrm{d}t + \gamma_{n1}^2\int_0^T \psi_n^{(n)}(t)^2\,\mathrm{d}t\Bigg]$$
$$-\frac{n(n+1)}{2}\Bigg[-\gamma_{n1}^2\int_0^T \psi_n^{(n)}(t)^2\,\mathrm{d}t + \gamma_{n1}\sum_{j=2}^{n} j\gamma_{nj}\int_0^T \psi_n^{(n+1)}(t)\psi_n^{(n-j)}(t)\,\mathrm{d}t$$
$$+ 2\gamma_{n1}\sum_{j=2}^{n}\gamma_{nj}\int_0^T \psi_n^{(n+1)}(t)\psi_n^{(n-j+1)}(t)\,\mathrm{d}t\Bigg]\Bigg\}. \tag{52}$$

Since $\gamma_{n1} = n(n+1)/2$, the first term on the right of (52) agrees with the first term on the right of (39). Therefore we need to apply the induction step only to the remaining terms. We do so in Lemma 2 (Appendix A), where we show that if the remaining terms on the right of (52) agree with the remaining terms on the right of (39) (with $R = 1$) for a certain n, they also do so for $n+1$, which completes the proof. □

6. Numerical examples

We shall now present several numerical examples, which demonstrate the high accuracy achieved by combining the nonreflecting boundary condition (4) with an adaptive finite element method. These test problems are far more challenging than those in previous studies (see, e.g., [14,15,29,30]), because of their much higher frequency content; hence, they are more typical of realistic applications. All test problems are time-dependent, three-dimensional, yet axisymmetric, that is φ-independent, so that Ω only needs to be two-dimensional. Thus we use the 2.5-D optimizations described in Section 4. All computations are performed in cartesian rather than spherical coordinates; hence, the inclusion of the origin into the computational domain Ω causes no particular difficulty.

6.1. Adaptive strategy

The numerical results are obtained with a program based on the *deal.II* finite element library [4–6]. It uses locally refined adaptive meshes on every time slab, which may vary from one time step to another, to efficiently track traveling small scale features—typical meshes are shown in Fig. 6. The successive refinement strategy attempts to equilibrate the a posteriori error indicator

$$\eta_K = h_K^{1/2}\|[a\partial_n u_h]\|_{\partial K}^2, \tag{53}$$

where h_K denotes the diameter of cell K and $[a\partial_n u_h]$ the jump of the conormal derivative of the numerical solution u_h across element interfaces. We refer to [24] for a rigorous derivation of (53) for the Laplace equation and to [6] for further details about the implementation. This refinement criterion is used everywhere inside Ω, but not along the artificial boundary $\mathscr{B}$—this point is discussed more extensively below in Section 6.3.

Because we use implicit time integration we need not satisfy a CFL condition; in fact, we usually violate it. Nevertheless, to preserve accuracy we choose for the current step size a fixed multiple of the step size mandated by the CFL condition. As a consequence, the spatial mesh refinement automatically results in adaptive time stepping.

Once the solution has been computed up to time T on a first set of grids, the grids at all time levels are refined according to the error indicator (53), while new time levels are possibly added. Then, the entire

numerical solution is recomputed up to time T on this new set of grids. Time steps are chosen to ensure that the local CFL-number, $c_K k/h_K$, for any spatial grid remains below a fixed upper bound; here c_K is the local wave speed in cell K. We call the entire set of spatial grids a "space–time mesh" and mean by "refinement" the space–time adaptive strategy described above. A more in-depth discussion of adaptivity for the wave equation can be found in [6].

The use of adapted nonuniform meshes precludes any convergence study with respect to a "typical" mesh size h. Instead, we shall show convergence results with respect to the *accumulated number of space–time degrees of freedom*, that is the number of time steps multiplied by the average number of degrees of freedom per time step. It is roughly proportional to the total computational work involved and therefore more precise a measure than any other quantity based on, say, a minimal or average mesh size.

6.2. Off-centered pulse

As a first example, we compute the purely outgoing wave field that originates from a localized off-centered pulse, defined by the initial conditions

$$u_0(\mathbf{x}) = \frac{f(|\mathbf{x}-\mathbf{x}_0|)}{|\mathbf{x}-\mathbf{x}_0|}, \quad v_0(\mathbf{x}) = \left[\frac{\partial_t f(|\mathbf{x}-\mathbf{x}_0|-t)}{|\mathbf{x}-\mathbf{x}_0|}\right]_{t=0}, \tag{54}$$

$$f(r) = \begin{cases} (27/4)s^3 r^2 (s-r)^2 & \text{for } 0 \leqslant r \leqslant r_0, \\ 0 & \text{otherwise.} \end{cases}$$

We choose $r_0 = 0.1$, $\mathbf{x}_0 = (0,0,0.8)^{\mathrm{T}}$, $R = 1$, and $\rho = a = 1$. Hence the propagation speed is $c = 1$ everywhere. The location of the initial pulse is indicated in Fig. 1. The exact solution $u(\mathbf{x},t) = f(|\mathbf{x}-\mathbf{x}_0|-t)/|\mathbf{x}-\mathbf{x}_0|$ corresponds to a purely outgoing spherically symmetric wave centered about $\mathbf{x}_0$, with maximal amplitude equal to one. Because the spatial extension of the initial disturbance, which is determined by r_0, is small, the frequency content of the exact solution is significant down to rather small length scales $\lambda \simeq (\operatorname{diam}\Omega)/30$. Moreover, on the right of Fig. 1 we observe the rather slow decay with n of the Fourier modes (Y_{nm}, u) on $\mathscr{B}$, up to $n \simeq 100$. Thus, we expect both a highly refined mesh and a large value of N to be prerequisites for any accurate numerical solution for this problem.

Let again $E(t) = E_R(t)$ denote the energy of the wave field within the computational domain Ω: $E_R(t) = \int_{|\mathbf{x}|<R} (\partial_t u)^2 + (\nabla u)^2 \,\mathrm{d}x$. Then a short calculation reveals that

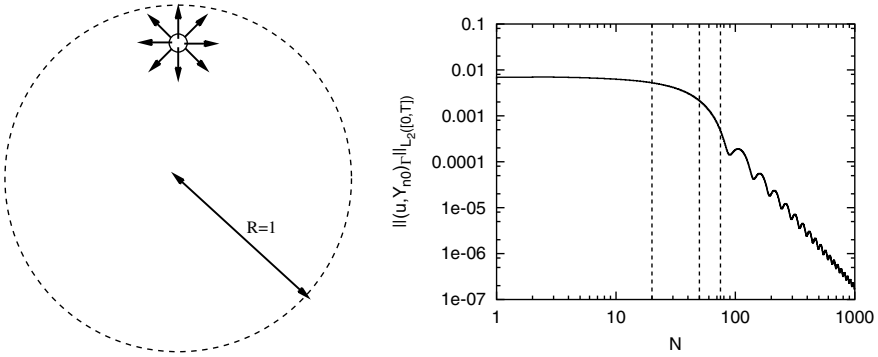

Fig. 1. Off-centered pulse. Computational domain (left); L_2-norm over $[0,T]$ of the nth Fourier mode on $\mathscr{B}$ (right). The vertical lines indicate three typical values for N used in the computations.

$$E_R(t) = 2\pi \int_0^\infty \left[2\big(f'(r-t)\big)^2 - \frac{2}{r} f(r-t) f'(r-t) + \frac{1}{r^2} f(r-t)^2 \right] \omega(r)\, \mathrm{d}r. \tag{55}$$

Here, $\omega(r)$ corresponds to the fraction of the surface of the sphere of radius r about $\mathbf{x}_0 = (0,0,z_0)$, which lies inside the centered sphere of radius R:

$$\omega(r) = \begin{cases} 1 & \text{for } r < R - z_0 = |\mathbf{x}_0|, \\ \dfrac{1}{2}\left(1 + \dfrac{R^2 - r^2 - z_0^2}{2 z_0 r}\right) & \text{for } R - z_0 \leqslant r \leqslant R + z_0, \\ 0 & \text{for } r > R + z_0. \end{cases}$$

With $z_0 = 0.8$, the (exact) wave field $u(\mathbf{x}, t)$ has entirely left Ω at $t = 1.8$, so that $E_R(t) = 0$ for $t \geqslant 1.8$.

We shall now compare the evolution of $E_R(t)$ for u, which we explicitly calculate from (55) with u_0, v_0 given by (54), with that obtained from the numerical solution. If the boundary condition imposed at $\mathscr{B}$ were perfectly absorbing, we would expect the numerical curve to approach the analytic one as the mesh size and the time step are successively refined. As shown in Fig. 2, however, the evolution curves for $E_R(t)$ obtained from increasingly accurate discretizations do not approach the correct limit, for any fixed value of N. Instead, they converge to the limiting behavior of a different initial-boundary value problem, with the boundary condition on $\mathscr{B}$ truncated at that fixed value of N. As N increases, however, we observe that the

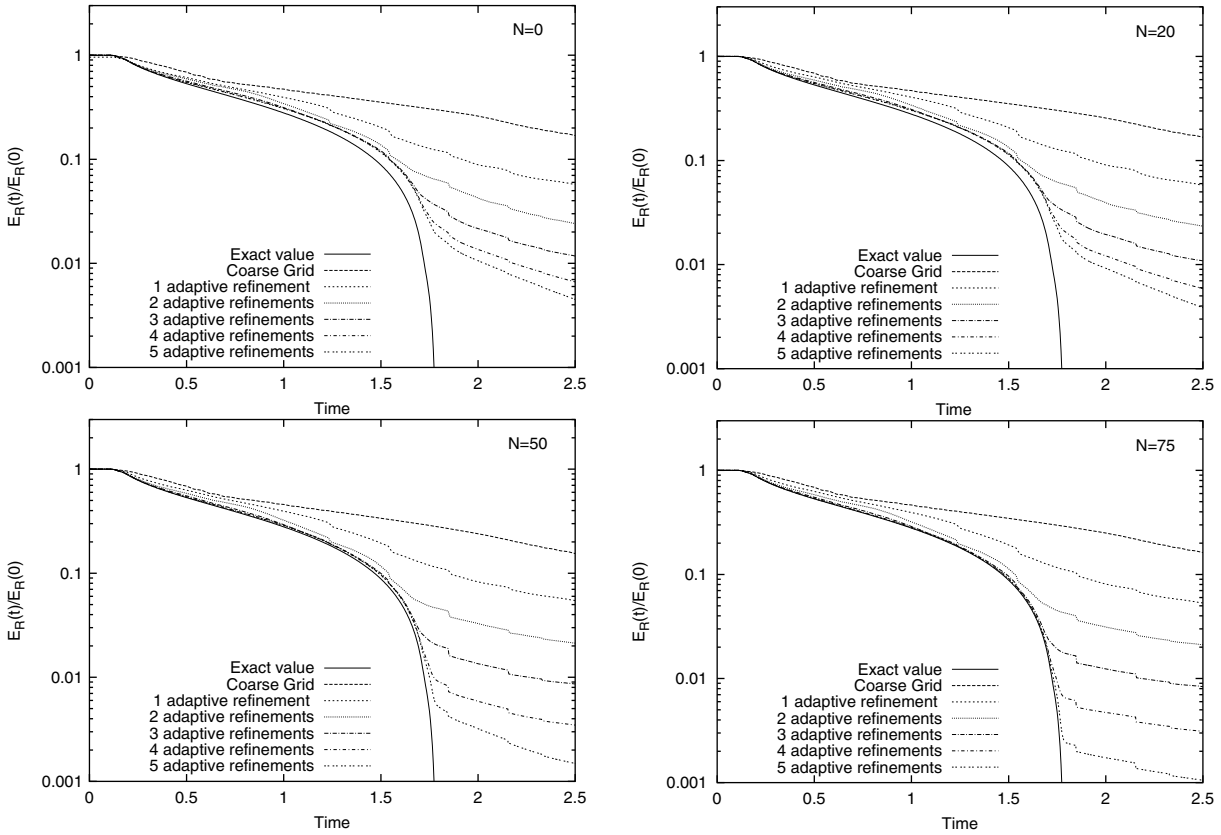

Fig. 2. Off-centered pulse. Decay of energy in the numerical solution for absorbing boundary conditions with orders $N = 0$ (top left), $N = 20$ (top right), $N = 50$ (bottom left), and $N = 75$ (bottom right).

limit curve for $h, k \to 0$ approaches the correct analytic behavior. Thus convergence of the numerical solution to that of the original problem stated in unbounded space is only achieved by reducing k and h, while *simultaneously* increasing N.

In Fig. 3 the fraction of energy $E_R(t = 1.8)/E_R(0)$ persisting in the numerical solution at time $t = 1.8$, is shown; by that time the exact solution has already left the domain. This residual energy consists of two independent contributions: $\mathscr{E}^{h,k}$, due to the discretization error, and $\mathscr{E}^N$, due to the truncation of the nonreflecting boundary condition at a finite N. Since $\mathscr{E}^N = \mathcal{O}(N^{-\beta_N})$ and $\mathscr{E}^{h,k} = \mathcal{O}(h^{\beta_h} + k^{\beta_k})$, where $\beta_N, \beta_h, \beta_k > 0$ are constants that depend on the particular discretization and the smoothness of the solution, the residual energy $E_R(t) = \mathscr{E}^{h,k} + \mathscr{E}^N$ will only converge to zero, if the mesh is refined while N is simultaneously increased. Otherwise, if N remains constant the energy decay stalls as $h, k \to 0$, an indication that the contribution of $\mathscr{E}^N$ now dominates in $E_R(t)$. For instance, a residual energy of nearly 2%, obtained with $N = 0$ on the finest mesh, corresponds to an error in the wave amplitude close to 15%, since the energy is quadratic in the wave amplitude. Yet by setting $N = 75$ in the boundary condition, the residual energy at $t = 1.8$ is about 10 times smaller.

6.3. Scattering from a sphere

We now consider scattering from a sphere of radius $r = 0.5$, as shown in Fig. 4. The impinging wave originates from a localized disturbance defined by initial conditions u_0, v_0, with u_0 as in (54) and $v_0 = 0$. Snapshots of the wave field are shown in Fig. 4 at times $t = 0.5, 1, 1.5$.

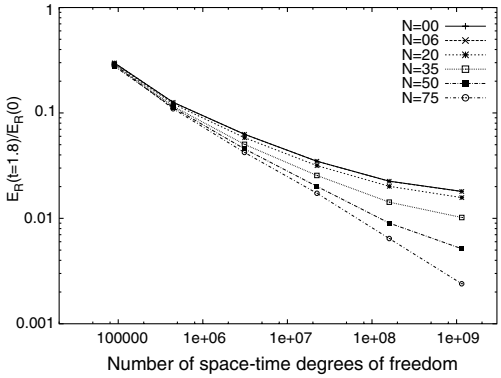

Fig. 3. Off-centered pulse. Fraction of the energy $E_R(t = 1.8)/E_R(0)$ in the numerical solution at a time, when the exact solution has left the domain entirely. The curves for $N = 0$ and $N = 6$ essentially coincide.

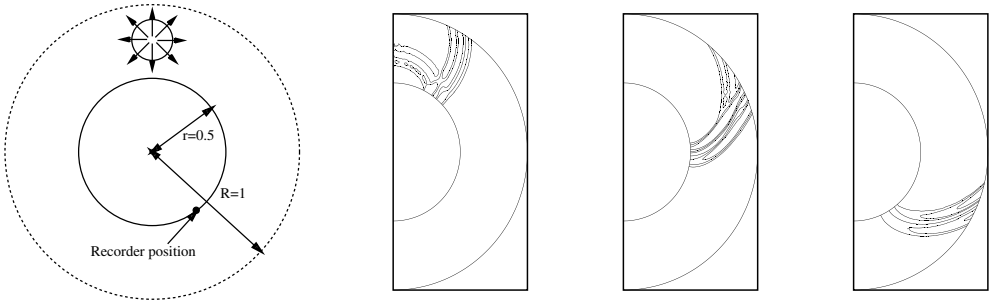

Fig. 4. Scattering from a sphere. Computational domain (left). Snapshots of the solution are shown at $t = 0.5$, 1, and 1.5.

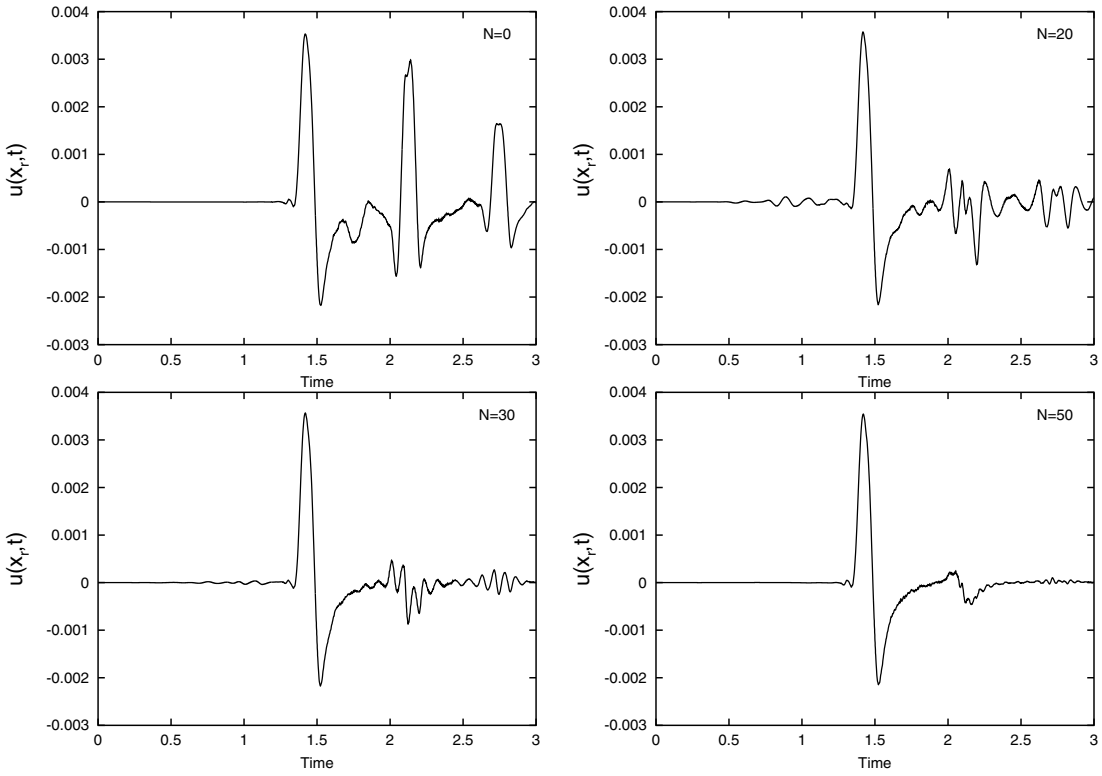

Fig. 5. Scattering from a sphere. Computed solution at the receiver's position for different values of N ($\max|u(t=0)|=1$).

In Fig. 5 the time evolution of the signal at the receiver, located at $x = 0.5\cos(3\pi/10)$ and $z = -0.5\sin(3\pi/10)$, is shown for different values of N—recall that the maximum of u at $t = 0$ is equal to one. For $N = 50$ the computed solution clearly displays the expected two peaks, where the first corresponds to arrival at $t = 1.33$ via the shorter (clockwise) travel distance, and the second corresponds to arrival at $t = 1.96$ via the longer (counter-clockwise) travel distance. Comparison of the different numerical solutions obtained with $N = 0, 20, 30, 50$, respectively, shows that the value of N hardly affects the first peak. However, as spurious reflections reach the receiver starting at $t = 1.77$, they entirely obscure the second (smaller) peak for moderate values of N. As N further increases up to fifty, the second peak in the signal eventually emerges while spurious reflections are successfully eliminated, an indication that errors due to the nonreflecting boundary condition no longer dominate the computed signal.

As the wave front impinges on $\mathscr{B}$ in the vicinity of the source, the refinement criterion based on the smoothness of the solution automatically adapts the mesh locally in that region. These small cells excite high-frequency modes, which are immediately transmitted along the entire artificial boundary $\mathscr{B}$, because of the global coupling of the unknowns induced by the nonreflecting boundary condition. Since these high-frequency modes are not well-represented in parts of $\mathscr{B}$ where the mesh is coarse, their superposition in (4) does not cancel out exactly there, as it would at the continuous level. As a consequence spurious precursors appear in the computed signal, even prior to the physical first arrival time—see the top right graph of Fig. 6. Similar difficulties are to be expected whenever nonreflecting boundary conditions that were derived at the continuous level, are applied to a numerical solution which is poorly resolved in some parts of the artificial boundary. A simple remedy to remove this artifact is the uniform refinement of the mesh along the entire

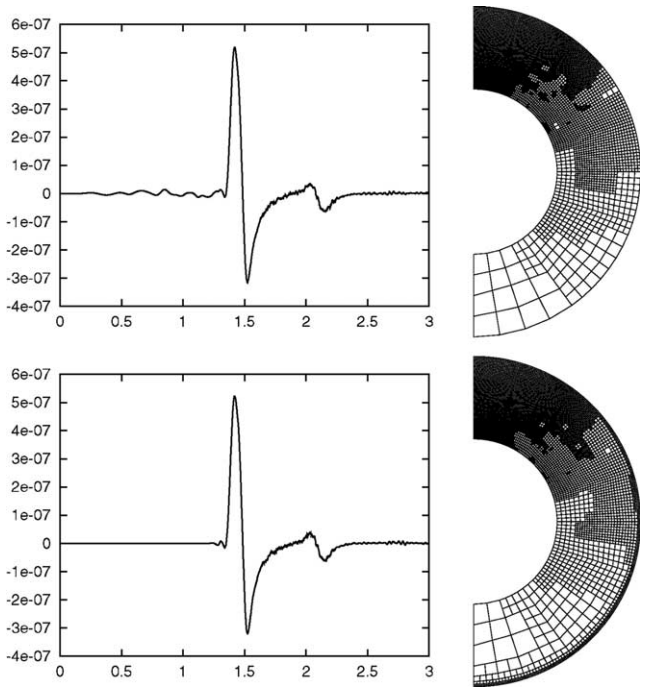

Fig. 6. Scattering from a sphere. Signal at the receiver's position (left), and a typical mesh (right). Standard refinement indicator (53) (top); with added refinement along the artificial boundary (bottom)—the spurious precursor has now disappeared.

artificial boundary. Fig. 6 shows a comparison of the signals computed either with or without additional refinement at $\mathscr{B}$, together with two typical resulting grids. With the added refinement the signal is flat until first arrival, while the spurious precursor has disappeared.

The requirement for additional refinement on $\mathscr{B}$ is clearly an artifact of the nonreflecting boundary condition. However, it does not significantly limit the applicability of adaptive meshes, since we only refine along the artificial boundary. Moreover, since the latter only is a lower-dimensional manifold, the total number of degrees of freedom increases by a mere few percent; therefore, it has no significant impact on the efficiency of our method either.

6.4. Scattering from complex geometry

As a last example we consider plane wave acoustic scattering from the wine glass-shaped acoustically "soft" obstacle displayed in Fig. 7. The incoming plane wave packet, $u_i(z,t)$, is given by

$$u_i(z,t) = \sin(k\tau)\sigma(\tau), \qquad \tau = z-(t-t_0), \quad t_0 = 2, \quad k = \frac{2\pi}{\lambda}, \quad \lambda = \frac{1}{3},$$

where $\sigma(\tau) = \exp(-1/(1-\tau^2))$ for $|\tau| < 1$; hence $u_i(z,t)$ is centered about $t = t_0$ and tapered to zero at $t = t_0 \pm 1$; outside the time window $[t_0 - 1, t_0 + 1]$ it is identically zero. Since the total wave field $u = u_i + u_s$ vanishes on the surface of the obstacle Γ, the (unknown) scattered field u_s satisfies the homogeneous wave equation outside Γ, with boundary condition

$$u_s(\mathbf{x},t) = -u_i(\mathbf{x},t) \quad \text{on } \Gamma.$$

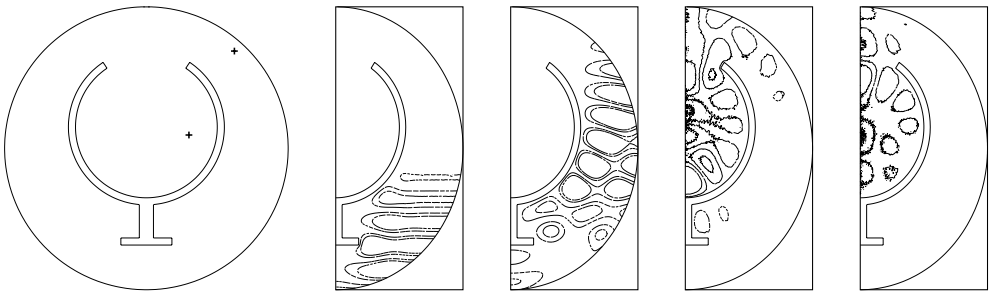

Fig. 7. Scattering from a complex geometry. Computational domain and obstacle; the locations of the two receivers are indicated by '+' signs (left). Isocontours of the solution at progressing times (middle to right).

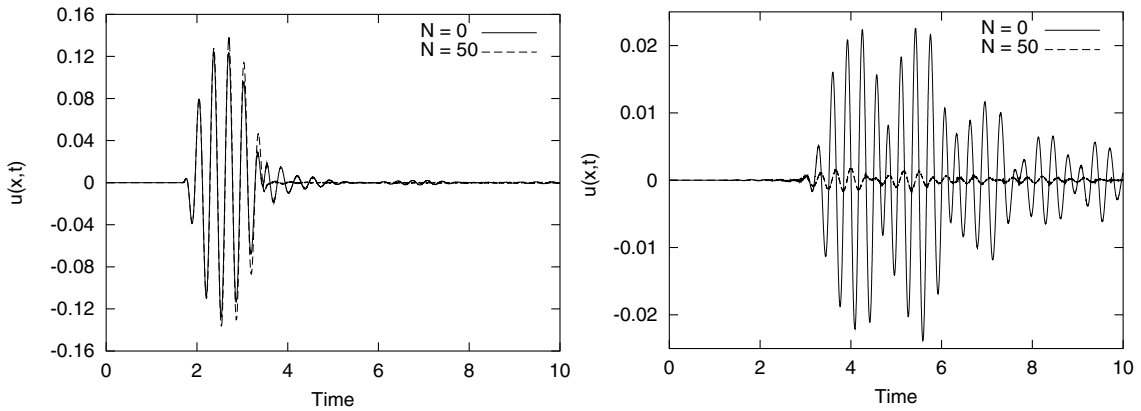

Fig. 8. Scattering from a complex geometry. Total wave field $u = u_i + u_s$ for $N = 0$ and $N = 50$: outside the obstacle (left), and inside the obstacle (right).

To evaluate the accuracy of the nonreflecting boundary conditions we shall compare for varying N the total acoustic field $u = u_i + u_s$ at the two locations shown in the left part of Fig. 7, inside and outside the obstacle. The complicated geometric features of the obstacle require higher order finite elements and boundary approximations—here we choose piecewise quadratic shape functions and a quadratic approximation of both interior and artificial boundaries. Both are available in the deal.II library [4,5].

In Fig. 8 the total acoustic wave field is shown at both receivers for both $N = 0$ and $N = 50$. Higher values of N did not lead to any further change in the numerical solutions. At the first location outside the obstacle, we observe for $N = 0$ about 20% error in the amplitude, together with some ringing effects at later times due to multiple spurious reflection. At the second location, however, the difference is more dramatic as spurious reflections from $\mathscr{B}$ begin to enter and resonate inside the "wine-glass". As a consequence, for $N = 0$ a spurious signal, about 10 times larger in amplitude than that obtained with $N = 50$, builds up inside the obstacle and completely masks the physical signal. Contrary to our expectation these computations demonstrate that accurate nonreflecting boundary conditions, which are imposed on the *outermost* artificial boundary, are in fact crucial to obtain accurate numerical results inside the *innermost* regions of the computational domain, even inside shielded structures and resonant cavities.

7. Conclusion

An efficient and highly accurate adaptive finite element method for time-dependent acoustic scattering in unbounded space has been proposed. It combines space–time adaptivity [6] with an exact nonreflecting boundary condition [14,15]. With the nonreflecting boundary condition the overall numerical scheme retains its optimal rate of convergence, as the error introduced at the artificial boundary can always be reduced below the discretization error due to the numerical methods used in the interior computational domain.

The overall efficiency of the method results from the capability to locally resolve propagating small-scale disturbances or geometric singularities, and to move the artificial boundary close to the scatterer without loss of accuracy. To avoid any stability constraints on the time-step because of small grid cells, we have opted for the implicit trapezoidal method in time. Although the use of an implicit time integrator couples all unknowns, both in the interior and at the boundary, the resulting system of linear equations can be decoupled and efficiently solved with (standard) preconditioned conjugate gradient iterations. Hence the additional work incurred by the use of the nonreflecting boundary condition remains marginal, even if high accuracy is required. Since the nonreflecting boundary condition naturally fits into the weak formulation at the continuous level, that is regardless of the discretization, neither unstructured meshes nor high-order finite elements cause any particular difficulty.

In practice the infinite series in the nonreflecting boundary condition (4) needs to be truncated at a finite value N. An interesting open question for future research is the derivation of a posteriori error estimates, similar to those in [6], yet with the artificial boundary condition included. Then, not only the mesh size and the time step, but also the value for N can be adapted a posteriori, so that the accuracy of the finite element approximation in the interior automatically matches that of the truncated nonreflecting boundary condition. The first author is currently investigating this issue and will report on this work elsewhere in the future [3].

Acknowledgements

During much of this work the first author was supported by the Graduiertenkolleg "Modellierung und Wissenschaftliches Rechnen in Mathematik und Naturwissenschaften" at the University of Heidelberg, Germany; this support is gratefully acknowledged.

Appendix A

Lemma 1. *For $n \geqslant 2$, let*

$$a_i = \frac{(n+i)(n+1-i)}{2i}, \quad i = 2, \ldots, n.$$

Then for all $2 \leqslant k \leqslant n$,

$$p_k = \prod_{j=k}^{n} a_j = \frac{(2n)!}{(n)!} \frac{1}{2^n \gamma_{n,k-1}}, \tag{A.1}$$

with γ_{nm} as in (40) (*see Proposition* 2).

Proof. The proof is by induction over k.

Case $k = 2$.

$$p_2 = \frac{(n+2)(n-1)}{2\cdot 2}\,\frac{(n+3)(n-2)}{2\cdot 3}\cdots\frac{(2n-1)2}{2(n-1)}\,\frac{2n\cdot 1}{2n} = \frac{(2n)!}{n!}\,\frac{1}{2^n\gamma_{n1}}.$$

Induction step. Suppose that (A.1) holds for k, $k \leqslant n-1$. We need to show that it holds for $k+1$, too. This follows immediately from

$$p_{k+1} = \frac{p_k}{a_k} = \frac{(2n)!}{n!}\,\frac{1}{2^n\gamma_{n,k-1}}\,\frac{1}{a_k} = \frac{(2n)!}{n!}\,\frac{1}{2^n\gamma_{nk}}. \qquad \square$$

Lemma 2. *Let* Ξ_{nm} *denote all terms but the first on the right of* (52). *If* Ξ_{nm} *satisfies*

$$\Xi_{nm} = -\left(\frac{(n+1)!}{(2n-1)!}\right)^2 2^{2n-5}\left[\sum_{k=0}^{n-1}(2k+1)\left(\sum_{j=0}^{k}\gamma_{kj}\psi_n^{(n-j)}(T)\right)^2 + (n+1)\left(\sum_{j=0}^{n}\gamma_{nj}\psi_n^{(n-j)}(T)\right)^2\right] \tag{A.2}$$

with $\boldsymbol{\psi} = \boldsymbol{\psi}_{nm}$ *for a certain* $n \geqslant 3$, *then* $\Xi_{n+1,m}$ *satisfies* (A.2), *with* n *replaced by* $n+1$ *and* $\boldsymbol{\psi} = \boldsymbol{\psi}_{n+1,m}$. *Note that the right of* (A.2) *coincides with all terms but the first on the right of* (39) *with* $R = 1$.

Proof. We assume that (A.2) holds for n and shall now show that it also holds for $n+1$. First, we let

$$\mu_{nj} = \frac{n+1+j}{n+1-j},$$

which satisfies the two useful identities,

$$\gamma_{n+1,j} = \mu_{nj}\gamma_{nj} \quad \text{and} \quad \gamma_{n+1,n+1} = (2n+1)\gamma_{nn}.$$

We now evaluate $\Xi_{n+1,m}$, which yields

$$\begin{aligned}
\Xi_{n+1,m} = \frac{1}{(2n+1)^2}\left(\frac{n!}{(2n)!}\right)^2 2^{2n}\Bigg\{ & \underline{\underline{-\gamma_{n1}^2\mu_{n1}^2\left(\psi_{n+1}^{(n+1)}(T) + \frac{(n+1)(n+2)}{2}\psi_{n+1}^{(n)}(T)\right)^2}} \\
& \underline{\underline{-\frac{1}{2}(n^2+3n)\gamma_{n1}^2\mu_{n1}^2\psi_{n+1}^{(n+1)}(T)^2 - \frac{1}{2}\left(\mu_{n1}\gamma_{n1}\psi_{n+1}^{(n+1)}(T) + \frac{(n+1)(n+2)}{2}\sum_{j=2}^{n}\gamma_{nj}\mu_{nj}\psi_{n+1}^{(n+1-j)}(T)\right)^2}} \\
& -\psi_{n+1}(T)\frac{(n+1)(n+2)}{2}(2n+1)\cdot\gamma_{nn}\left(\mu_{n1}\gamma_{n1}\psi_{n+1}^{(n+1)}(T) + \frac{(n+1)(n+2)}{2}\sum_{j=2}^{n}\gamma_{nj}\mu_{nj}\psi_{n+1}^{(n+1-j)}(T)\right). \\
& -\left(\frac{(n+1)(n+2)}{2}\right)^2\Bigg[\frac{(2n+1)^2}{2}\gamma_{nn}^2\psi_{n+1}(T)^2 + \underline{\int_0^T\left(\sum_{j=2}^{n}\gamma_{nj}\mu_{nj}\psi_{n+1}^{(n+2-j)}(t)\right)^2 \mathrm{d}t} \\
& + 2(2n+1)\gamma_{nn}\int_0^T\psi_{n+1}^{(1)}(t)\sum_{j=2}^{n}\gamma_{nj}\mu_{nj}\psi_{n+1}^{(n+2-j)}(t)\,\mathrm{d}t + (2n+1)^2\gamma_{nn}^2\cdot\int_0^T\psi_{n+1}^{(1)}(t)^2\,\mathrm{d}t \\
& \underline{\underline{+\mu_{n1}\gamma_{n1}\sum_{j=2}^{n}\gamma_{nj}\mu_{nj}\int_0^T\psi_{n+1}^{(n)}(t)\psi_{n+1}^{(n+2-j)}(t)\,\mathrm{d}t}}
\end{aligned}$$

$$
\begin{aligned}
&+\mu_{n1}\gamma_{n1}(2n+1)\cdot\gamma_{nn}\int_0^T \psi_{n+1}^{(1)}(t)\psi_{n+1}^{(n)}(t)\,\mathrm{d}t+\underline{\underline{\mu_{n1}\gamma_{n1}\sum_{j=2}^{n} j\gamma_{nj}\mu_{nj}\int_0^T \psi_{n+1}^{(n+1)}(t)\psi_{n+1}^{(n+1-j)}(t)\,\mathrm{d}t}}\\
&+\mu_{n1}\gamma_{n1}(2n+1)\gamma_{nn}(n+1)\int_0^T \psi_{n+1}(t)\psi_{n+1}^{(n+1)}(t)\,\mathrm{d}t+\underline{\underline{\int_0^T \sum_{j=2}^{n}\gamma_{nj}\mu_{nj}\psi_{n+1}^{(n+2-j)}(t)\sum_{j=2}^{n} j\gamma_{nj}\mu_{nj}\psi_{n+1}^{(n+1-j)}(t)\,\mathrm{d}t}}\\
&+(2n+1)\gamma_{nn}\cdot\int_0^T \psi_{n+1}^{(1)}(t)\sum_{j=2}^{n} j\gamma_{nj}\mu_{nj}\psi_{n+1}^{(n+1-j)}(t)\,\mathrm{d}t\\
&+(2n+1)\gamma_{nn}(n+1)\int_0^T\left(\psi_{n+1}(t)\cdot\sum_{j=2}^{n}\gamma_{nj}\mu_{nj}\psi_{n+1}^{(n+2-j)}(t)\right)\mathrm{d}t\\
&+(2n+1)^2\gamma_{nn}^2(n+1)\int_0^T \psi_{n+1}(t)\psi_{n+1}^{(1)}(t)\,\mathrm{d}t+\underline{\underline{\mu_{n1}\gamma_{n1}\psi_{n+1}^{(n)}(T)\sum_{j=2}^{n}\gamma_{nj}\mu_{nj}\psi_{n+1}^{(n+1-j)}(T)}}\\
&+\mu_{n1}\gamma_{n1}(2n+1)\gamma_{nn}\psi_{n+1}^{(n)}(T)\psi_{n+1}(T)+\underline{\underline{2\mu_{n1}\gamma_{n1}\sum_{j=2}^{n}\gamma_{nj}\mu_{nj}\int_0^T \psi_{n+1}^{(n+1)}(t)\psi_{n+1}^{(n+2-j)}(t)\,\mathrm{d}t}}\\
&+2\mu_{n1}\gamma_{n1}(2n+1)\gamma_{nn}\cdot\int_0^T \psi_{n+1}^{(1)}(t)\psi_{n+1}^{(n+1)}(t)\,\mathrm{d}t+\underline{\underline{\mu_{n1}^2\gamma_{n1}^2\int_0^T \psi_{n+1}^{(n+1)}(t)^2\,\mathrm{d}t}}\Bigg]\\
&-\frac{(n+1)(n+2)}{2}\cdot\Bigg[\underline{\underline{-\mu_{n1}^2\gamma_{n1}^2\int_0^T \psi_{n+1}^{(n+1)}(t)^2\,\mathrm{d}t+\mu_{n1}\gamma_{n1}\sum_{j=2}^{n} j\gamma_{nj}\mu_{nj}\int_0^T \psi_{n+1}^{(n+2)}(t)\psi_{n+1}^{(n+1-j)}(t)\,\mathrm{d}t.}}\\
&+\mu_{n1}(2n+1)\gamma_{nn}(n+1)\gamma_{n1}\int_0^T \psi_{n+1}^{(n+2)}(t)\psi_{n+1}(t)\,\mathrm{d}t+\underline{\underline{2\mu_{n1}\gamma_{n1}\sum_{j=2}^{n}\gamma_{nj}\mu_{nj}\cdot\int_0^T \psi_{n+1}^{(n+2)}(t)\psi_{n+1}^{(n+2-j)}(t)\,\mathrm{d}t}}\\
&+2\mu_{n1}\gamma_{n1}(2n+1)\gamma_{nn}\int_0^T \psi_{n+1}^{(1)}(t)\psi_{n+1}^{(n+2)}(t)\,\mathrm{d}t\Bigg]\Bigg\}. \qquad \text{(A.3)}
\end{aligned}
$$

To further simplify the notation we introduce

$$v_{nj}=\frac{2j}{n+1-j}.$$

Note that $\mu_{nj}=1+v_{nj}$. We now concentrate on the underlined terms in (A.3). By further adding and subtracting terms in (A.3) we attempt to make the coefficients before the sums and integrals coincide with the corresponding coefficients on the right of (52). Thus we rewrite *only the underlined terms* in (A.3) as

$$
\begin{aligned}
&\frac{\mu_{n1}^2}{(2n+1)^2}2^{2n}\left(\frac{n!}{(2n)!}\right)^2\Bigg\{-\boldsymbol{\gamma_{n1}^2}\left(\boldsymbol{\psi_{n+1}^{(n+1)}}(\boldsymbol{T})+\frac{\boldsymbol{n(n+1)}}{\boldsymbol{2}}\boldsymbol{\psi_{n+1}^{(n)}}(\boldsymbol{T})\right)^{\boldsymbol{2}}\\
&-2(n+1)\gamma_{n1}^2\psi_{n+1}^{(n)}(T)\left(\psi_{n+1}^{(n+1)}(T)+\frac{n(n+1)}{2}\psi_{n+1}^{(n)}(T)\right)\\
&-(n+1)^2\gamma_{n1}^2\psi_{n+1}^{(n)}(T)^2-\frac{\boldsymbol{1}}{\boldsymbol{2}}\boldsymbol{(n^2+n-2)\gamma_{n1}^2\psi_{n+1}^{(n+1)}}(\boldsymbol{T})^{\boldsymbol{2}}\\
&-(n+1)\gamma_{n1}^2\psi_{n+1}^{(n+1)}(T)^2-\frac{\boldsymbol{1}}{\boldsymbol{2}}\left(\boldsymbol{\gamma_{n1}\psi_{n+1}^{(n+1)}}(\boldsymbol{T})+\frac{\boldsymbol{n(n+1)}}{\boldsymbol{2}}\sum_{\boldsymbol{j=2}}^{\boldsymbol{n}}\boldsymbol{\gamma_{nj}\psi_{n+1}^{(n+1-j)}}(\boldsymbol{T})\right)^{\boldsymbol{2}}
\end{aligned}
$$

$$
\begin{aligned}
&-\frac{n(n+1)}{2}\left(\gamma_{n1}\psi_{n+1}^{(n+1)}(T)+\frac{n(n+1)}{2}\sum_{j=2}^{n}\gamma_{nj}\psi_{n+1}^{(n+1-j)}(T)\right)\sum_{j=2}^{n}\gamma_{nj}v_{nj}\psi_{n+1}^{(n+1-j)}(T)\\
&-\left(\frac{n(n+1)}{2}\right)^2\left[\frac{1}{2}\left(\sum_{j=2}^{n}\gamma_{nj}v_{nj}\psi_{n+1}^{(n+1-j)}(T)\right)^2+\int_0^T\left(\sum_{\boldsymbol{j=2}}^{\boldsymbol{n}}\boldsymbol{\gamma_{nj}\psi_{n+1}^{(n+2-j)}(t)}\right)^{\mathbf{2}}\mathbf{d}\boldsymbol{t}\right.\\
&+2\int_0^T\sum_{j=2}^{n}\gamma_{nj}\psi_{n+1}^{(n+2-j)}(t)\sum_{j=2}^{n}\gamma_{nj}v_{nj}\psi_{n+1}^{(n+2-j)}(t)\,\mathrm{d}t\\
&+\int_0^T\left(\sum_{j=2}^{n}\gamma_{nj}v_{nj}\psi_{n+1}^{(n+2-j)}(t)\right)^2\mathrm{d}t+\boldsymbol{\gamma_{n1}\sum_{j=2}^{n}\gamma_{nj}\int_0^T\psi_{n+1}^{(n)}(t)\psi_{n+1}^{(n+2-j)}(t)\,\mathbf{d}t}\\
&+v_{n1}\gamma_{n1}\sum_{j=2}^{n}\gamma_{nj}\mu_{nj}\int_0^T\psi_{n+1}^{(n)}(t)\psi_{n+1}^{(n+2-j)}(t)\,\mathrm{d}t\\
&+\gamma_{n1}\sum_{j=2}^{n}v_{nj}\int_0^T\psi_{n+1}^{(n)}(t)\psi_{n+1}^{(n+2-j)}(t)\,\mathrm{d}t\\
&+\boldsymbol{\gamma_{n1}\sum_{j=2}^{n}j\gamma_{nj}\int_0^T\psi_{n+1}^{(n+1)}(t)\psi_{n+1}^{(n+1-j)}(t)\,\mathbf{d}t}+v_{n1}\gamma_{n1}\sum_{j=2}^{n}j\gamma_{nj}\mu_{nj}\int_0^T\psi_{n+1}^{(n+1)}(t)\psi_{n+1}^{(n+1-j)}(t)\,\mathrm{d}t\\
&+\gamma_{n1}\sum_{j=2}^{n}j\gamma_{nj}v_{nj}\int_0^T\psi_{n+1}^{(n+1)}(t)\psi_{n+1}^{(n+1-j)}(t)\,\mathrm{d}t+\int_0^T\boldsymbol{\sum_{j=2}^{n}\gamma_{nj}\psi_{n+1}^{(n+2-j)}(t)\sum_{j=2}^{n}j\gamma_{nj}\psi_{n+1}^{(n+1-j)}(t)\,\mathbf{d}t}\\
&+\int_0^T\left(\sum_{j=2}^{n}\gamma_{nj}v_{nj}\psi_{n+1}^{(n+2-j)}(t)\cdot\sum_{j=2}^{n}j\gamma_{nj}\psi_{n+1}^{(n+1-j)}(t)\right)\mathrm{d}t+\int_0^T\sum_{j=2}^{n}\gamma_{nj}\psi_{n+1}^{(n+2-j)}(t)\sum_{j=2}^{n}j\gamma_{nj}v_{nj}\psi_{n+1}^{(n+1-j)}(t)\,\mathrm{d}t\\
&+\int_0^T\sum_{j=2}^{n}\gamma_{nj}v_{nj}\psi_{n+1}^{(n+2-j)}(t)\sum_{j=2}^{n}j\gamma_{nj}v_{nj}\psi_{n+1}^{(n+1-j)}(t)\,\mathrm{d}t+\boldsymbol{\gamma_{n1}\psi_{n+1}^{(n)}(T)\sum_{j=2}^{n}\gamma_{nj}\psi_{n+1}^{(n+1-j)}(T)}\\
&+v_{n1}\gamma_{n1}\sum_{j=2}^{n}\gamma_{nj}\mu_{nj}\psi_{n+1}^{(n)}(T)\psi_{n+1}^{(n+1-j)}(T)+\gamma_{n1}\psi_{n+1}^{(n)}(T)\sum_{j=2}^{n}\gamma_{nj}v_{nj}\psi_{n+1}^{(n+1-j)}(T)\\
&+\boldsymbol{2\gamma_{n1}\sum_{j=2}^{n}\gamma_{nj}\int_0^T\psi_{n+1}^{(n+1)}(t)\psi_{n+1}^{(n+2-j)}(t)\,\mathbf{d}t}+2v_{n1}\gamma_{n1}\sum_{j=2}^{n}\gamma_{nj}\mu_{nj}\int_0^T\psi_{n+1}^{(n+1)}(t)\psi_{n+1}^{(n+2-j)}(t)\,\mathrm{d}t\\
&\left.+2\gamma_{n1}\sum_{j=2}^{n}\gamma_{nj}v_{nj}\int_0^T\psi_{n+1}^{(n+1)}(t)\psi_{n+1}^{(n+2-j)}(t)\,\mathrm{d}t+\boldsymbol{\gamma_{n1}^2\int_0^T\psi_{n+1}^{(n+1)}(t)^2\,\mathbf{d}t}+v_{n1}^2(n+1)\gamma_{n1}^2\int_0^T\psi_{n+1}^{(n+1)}(t)^2\,\mathrm{d}t\right]\\
&-\frac{n(n+1)}{2}\left[-\boldsymbol{\gamma_{n1}^2\int_0^T\psi_{n+1}^{(n+1)}(t)^2\,\mathbf{d}t}-v_{n1}\gamma_{n1}^2\int_0^T\psi_{n+1}^{(n+1)}(t)^2\,\mathrm{d}t+\boldsymbol{\gamma_{n1}\sum_{j=2}^{n}j\gamma_{nj}\int_0^T\psi_{n+1}^{(n+2)}(t)\psi_{n+1}^{(n+1-j)}(t)\,\mathbf{d}t}\right.\\
&+\gamma_{n1}\sum_{j=2}^{n}j\gamma_{nj}v_{nj}\int_0^T\psi_{n+1}^{(n+2)}(t)\psi_{n+1}^{(n+1-j)}(t)\,\mathrm{d}t+\boldsymbol{2\gamma_{n1}\sum_{j=2}^{n}\gamma_{nj}\int_0^T\left(\psi_{n+1}^{(n+2)}(t)\cdot\psi_{n+1}^{(n+2-j)}(t)\right)\mathbf{d}t}\\
&\left.\left.+2\gamma_{n1}\sum_{j=2}^{n}\gamma_{nj}v_{nj}\int_0^T\psi_{n+1}^{(n+2)}(t)\psi_{n+1}^{(n+2-j)}(t)\,\mathrm{d}t\right]\right\}
\end{aligned}
\tag{A.4}
$$

If we set $\psi_n(t) = \psi'_{n+1}(t)$ in Ξ_{nm} and multiply the resulting expression by $\mu_{n1}^2/(2n+1)^2 = (n+2)^2/n^2(2n+1)^2$, we find precisely the bold terms of (A.4). Hence, we can now apply the induction assumption (A.2) to them and thereby replace the **bold terms** in (A.4) by

$$-\frac{(n+2)^2}{n^2(2n+1)^2}\left(\frac{(n+1)!}{(2n-1)!}\right)^2 2^{2n-5}\left[\sum_{k=0}^{n-1}(2k+1)\left(\sum_{j=0}^{k}\gamma_{kj}\psi_{n+1}^{(n+1-j)}(T)\right)^2 + (n+1)\left(\sum_{j=0}^{n}\gamma_{nj}\psi_{n+1}^{(n+1-j)}(T)\right)^2\right]. \tag{A.5}$$

In fact, (A.5) nearly looks like (A.2). Indeed, if we add

$$-\left(\frac{(n+2)!}{(2n+1)!}\right)^2 2^{2n-3}\left[n\left(\sum_{j=0}^{n}\gamma_{nj}\psi_{n+1}^{(n+1-j)}(T)\right)^2 + (n+2)\left(\sum_{j=0}^{n+1}\gamma_{(n+1)j}\psi_{n+1}^{(n+1-j)}(T)\right)^2\right] \tag{A.6}$$

to (A.5) we obtain (A.2), with n replaced by $n+1$. Therefore, to conclude the proof we only need to show that the sum of all remaining terms, those either not underlined in (A.3) or not bold in (A.4), is equal to (A.6). We omit these straightforward but cumbersome calculations here. □

References

[1] A.K. Aziz, P. Monk, Continuous finite elements in space and time for the heat equation, Math. Comput. 52 (1989) 255–274.
[2] L. Bales, I. Lasiecka, Continuous finite elements in space and time for the nonhomogeneous wave equation, Comput. Math. Appl. 27 (3) (1994) 91–102.
[3] W. Bangerth, Fully adaptive finite element discretizations and error estimation for nonreflecting boundary conditions, in preparation.
[4] W. Bangerth, R. Hartmann, G. Kanschat, deal.II Differential Equations Analysis Library, Technical Reference, IWR, Universität Heidelberg, 2004. Available from <http://gaia.iwr.uni-heidelberg.de/~deal/>.
[5] W. Bangerth, G. Kanschat, Concepts for object-oriented finite element software—the deal.II library, Preprint 99-43, SFB 359, Universität Heidelberg, October 1999.
[6] W. Bangerth, R. Rannacher, Finite element approximation of the acoustic wave equation: error control and mesh adaptation, East–West J. Numer. Math. 7 (4) (1999) 263–282.
[7] W. Bangerth, R. Rannacher, Adaptive finite element techniques for the acoustic wave equation, J. Comput. Acoustics 9 (2) (2001) 575–591.
[8] A. Bayliss, E. Turkel, Radiation boundary conditions for wave-like equations, Commun. Pure Appl. Math. 33 (1980) 707–725.
[9] T. Belytschko, M. Tabbara, H-adaptive finite element methods for dynamic problems, with emphasis on localization, Internat. J. Numer. Methods Engrg. 36 (1993) 4245–4265.
[10] J.-P. Bérenger, A perfectly matched layer approach for the absorption of electromagnetic waves, J. Comput. Phys. 114 (1994) 185–200.
[11] B. Engquist, A. Majda, Absorbing boundary conditions for the numerical simulation of waves, Math. Comput. 31 (1977) 629–651.
[12] D.A. French, A space–time finite element method for the wave equation, Comput. Methods Appl. Mech. Engrg. 107 (1993) 145–157.
[13] M.J. Grote, Nonreflecting boundary conditions for elastodynamic scattering, J. Comput. Phys. 161 (2000) 331–353.
[14] M.J. Grote, J.B. Keller, Exact nonreflecting boundary condition for the time dependent wave equation, SIAM J. Appl. Math. 55 (1995) 280–297.
[15] M.J. Grote, J.B. Keller, Nonreflecting boundary conditions for time dependent scattering, J. Comput. Phys. 127 (1996) 52–65.
[16] M.J. Grote, J.B. Keller, Nonreflecting boundary conditions for Maxwell's equations, J. Comput. Phys. 139 (1998) 327–342.
[17] M.J. Grote, J.B. Keller, Exact nonreflecting boundary condition for elastic waves, SIAM J. Appl. Math. 60 (2000) 803–819.
[18] M.J. Grote, C. Kirsch, Far-field evaluation via nonreflecting boundary conditions, in: T. Hou, E. Tadmor (Eds.), Proc. of the Ninth Intern. Conf. on Hyperb. Problems, Springer Verlag, 2003, pp. 195–204.
[19] T. Hagstrom, Radiation boundary conditions for the numerical simulation of waves, in: A. Iserles (Ed.), Acta Numerica 1999, vol. 8, Cambridge University Press, 1999, pp. 47–106.

[20] T. Hagstrom, S.I. Hariharan, A formulation of asymptotic and exact boundary conditions using local operators, Appl. Numer. Math. 27 (1998) 403–416.
[21] T.J.R. Hughes, G.M. Hulbert, Space-time fem for elastodynamics and error estimates, Comput. Methods Appl. Mech. Engrg. 66 (1988) 339–363.
[22] C.A. Issa, K. Balasubramaniam, K. Srirengan, Adaptive hp-finite element for transient analysis, Appl. Math. Comput. 65 (1994) 315–334.
[23] C. Johnson, Discontinuous Galerkin finite element methods for second order hyperbolic problems, Comput. Methods Appl. Mech. Engrg. 107 (1993) 117–129.
[24] D.W. Kelly, J.P. de S.R. Gago, O.C. Zienkiewicz, I. Babuška, A posteriori error analysis and adaptive processes in the finite element method: Part I—error analysis, Internat. J. Numer. Methods Engrg. 19 (1983) 1593–1619.
[25] X.D. Li, N.-E. Wiberg, Implementation and adaptivity of a space–time finite element method for structural dynamics, Comput. Methods Appl. Mech. Engrg. 156 (1998) 211–229.
[26] Q. Qi, T.L. Geers, Evaluation of the perfectly matched layer for computational acoustics, J. Comput. Phys. 139 (1996) 166–183.
[27] A. Safjan, J.T. Oden, High-order Taylor–Galerkin and adaptive *h–p* methods for second-order hyperbolic systems: application to elastodynamics, Comput. Methods Appl. Mech. Engrg. 103 (1993) 187–230.
[28] E. Süli, C. Wilkins, Adaptive finite element methods for the damped wave equation, Report no. 96/23, Oxford University Computing Laboratory, 1996.
[29] L.L. Thompson, R. Huan, Finite element formulation of exact nonreflecting boundary conditions for the time-dependent wave equation, Internat. J. Numer. Methods. Engrg. 45 (1999) 1607–1630.
[30] L.L. Thompson, R. Huan, Implementation of exact non-reflecting boundary conditions in the finite element method for the time-dependent wave equation, Comput. Methods Appl. Mech. Engrg. 187 (2000) 137–159.
[31] N.-E. Wiberg, L.F. Zeng, X.D. Li, Error estimation and adaptivity in elastodynamics, Comput. Methods Appl. Mech. Engrg. 101 (1992) 369–395.